Nuclear dependence of Transverse momentum distributions for Drell-Yan, J/Ψ, and Ψ' production in p+p collisions at $\sqrt{s}$=15.5 GeV

Su-Yin Grass Wang

Advisors:
Dr. Rurng-Sheng Guo
Dr. Wen-Chen Chang

Submitted as partial fulfillment of the requirements
for the degree of Doctor of Philosophy
in the Department of Physics of the
National Kaohsiung Normal University

January, 2016

國立高雄師範大學博碩士論文著作權歸屬確認書

論文名稱： Nuclear dependence of transverse momentum distributions for Drell-Yan, J/Ψ, and Ψ' production in p+p collisions at sqrt(s) =15.5 GeV

指導教授： 郭榮升 老師

共同指導教授： 章文箴 老師

研究生： 王素音

學系／研究所： 物理學系

論文種類：☒博士論文　　　□碩士論文

　　為釐清學位論文之著作權歸屬，特立本確認書。博、碩士研究生所撰寫之學位論文，如指導教授及共同指導教授（以下簡稱指導教授們）僅為觀念之指導，並未實際參與內容之撰寫，依著作權法規定，研究生為本論文之著作人，單獨擁有著作權。但如指導教授們不僅為觀念的指導，且參與內容之表達，進而與研究生共同完成論文，且各人之創作，不能分離利用者，則為共同著作，研究生、指導教授們為論文的共同著作人並共同享有著作權，此等共同著作權（包括著作財產權及著作人格權）的行使，即應取得研究生、指導教授們之共同同意後，始得為之。

　　依上述原則，本論文之著作權歸屬(請勾選)：

□ 研究生單獨享有

□ 研究生與指導教授共同享有

☒ 研究生、指導教授及共同指導教授共同享有

研究生簽名：＿＿＿＿＿＿＿ 日期：105 年 1 月 30 日

指導教授簽名：＿＿＿＿＿＿＿ 日期：105 年 2 月 1 日

共同指導教授簽名：＿＿＿＿＿＿＿ 日期：105 年 1 月 30 日

備註：論文公開與否應由學生與指導教授取得共識為原則。

高 雄 師 範 大 學

博碩士論文全文上網授權書

(提供授權人裝訂於紙本論文書名頁之次頁用)

本授權書所授權之論文為授權人在高雄師範大學
物理學系 104 學年度第一學期取得博士學位之論文。

論文題目：

Nuclear dependence of transverse momentum distributions for
Drell-Yan, J/ Ψ , and Ψ ' production
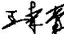in p+p collisions at sqrt(s) =15.5 GeV
指導教授：郭榮升,章文箴

■ 同意

本人同意上開著作之電子檔，無償授權國立高雄師範大學，不限時
間、形式與次數，以微縮、數位化或其他方式進行重製作為典藏之
用，並在合理範圍內，提供第三者閱覽、下載及列印。

論文全文上載網路公開之範圍及時間：

校內區域網路	■ 立即公開
校外網際網路	■ 不公開

著作權歸屬人簽名：　　　　王幸蓉　　　　　章文箴

(應同著作權歸屬確認書)

中 華 民 國 　　　 年 　　　 月 　　　 日

備註：

1.上述各項均為非專屬授權，立書人仍擁有上述授權著作之著作權。
立書人擔保本著作為立書人所創作之著作，有權依本授權書內容進行
各項授權，且未侵害任何第三人之智慧財產權。如有侵害他人權益及
觸犯法律之情事，立書人願自行負責一切法律責任，被授權人一概無
涉。

2.本授權書之授權範圍僅限電子檔，紙本論文部分依著作權法第 **15** 條
第 **3** 款之規定，採推定原則即預設同意圖書館得公開上架閱覽，如有
申請專利或投稿等考量，須另行加填紙本暫緩上架申請書。

國立高雄師範大學博士班研究生

論文口試審定書

物理學系博士班　　王素音　　所提之論文

Nuclear dependence of Transverse momentum distributions for Drell-Yan, J/Ψ , and Ψ ' production in p+p collisions at sqrt(s) =15.5 GeV

經下列委員口試及審議通過，特此證明：

口 試 委 員

指 導 教 授

系 主 任

中 華 民 國 一〇五 年 一 月 十一 日

致謝/ Acknowledgments

as my official advisor in Fermilab, who always gives good advice and great help. I would also like to thank the senior physicist, Don, Paul, and Chuck. They come to the counting house very often and always give students good advice. The very special thanks go out to Kaz, he is also my best friend. His expertise, understanding, and patience, added considerably to my graduate experience. I would like to thank the senior Taiwanese physicist, Yen-Chu and Ting. They help me a lot especially when I just arrived the US. I would also like to thank Japanese Group, especially Kenichi, Shou, and Kei. You are not just nice lab-mates, you are also amazing roommates. I must also acknowledge the young companions, all the graduate students in SeaQuest, who shared with me in the busy jobs and nice experiences. I would also like to thank my friends in the big Chicago area for bringing me the nice memory in the US.

最後，我要感謝媽媽，John Bay，和我的親朋好友們。當然還有婉玉，立璇，詠竹，Eva，Emily，Wendy, 因為你們的支持與陪伴，我才能順利走過了這一段旅程，謝謝你們。

Abstract

The suppression of J/Ψ and Ψ' production due to the plasmas screening of strong interaction has been considered as one of the important signatures of the formation of quark-gluon-plasma in the nucleus-nucleus collisions. In order to establish the baseline of similar suppression effect caused by the cold nuclear matter, the measurement of nuclear dependence of transverse momentum spectrum of J/Ψ, Ψ' and Drell-Yan production in the proton-nucleus collisions is essential. Other than understanding the absorption of charmonium in the nuclear medium, it also provides valuable information of production mechanisms for J/Ψ and Ψ' and the interaction of fast-moving partons with the nuclear medium before the hard collisions. We performed such measurement in SeaQuest E906 experiment at Fermilab with 120-GeV proton beams. By comparison with the results of similar measurement by E772 and E866 with 800-GeV proton beams, we observe no change in the production and absorption of J/Ψ and Ψ' and slightly stronger initial-state interaction for quarks with nuclear medium at low energies.

II

Contents

List of Figures

List of Tables

Chapter 1

Introduction

Fermilab E-906/SeaQuest experiment is the latest one of a series in fixed target Drell-Yan experiments. The Drell-Yan process is the production of a di-lepton pair decayed from the vertual photon produced from annihilation of quark and antiquark in the interactions of hadrons. The Drell-Yan process is a clean and important approach to the quark and antiquark structure of nucleons. Utilizing the high-intensity 120-GeV proton beam from the Main Injector at Fermilab, the SeaQuest experiment is able to determine both the partonic structure of the nucleon in the large momentum-fraction (x) region as well as the modifications of this structure inside the nucleus [1].

This Chapter introduces the background knowledge from standard model to QCD, as well as Deep-Inelastic Scattering, Drell-Yan

process, J/Ψ and Ψ' production and its production mechanism; ends with what E772 and E886 found as the previous version of E906-SeaQuest experiment, and what SeaQuest would like to compare with them.

1.1   Standard model

The object of particle physics is to understand the basic structure and laws in nature, all the way from the largest dimension in the universe, formation of galaxies and stars, all the way down to the smallest dimension to the microcosm. Historically we knew about all the different elements you knew about, such as helium, hydrogen, oxygen, gold, and so on. They are all made of different atoms. A great simplification was made when we realized that all atoms are just made by three particles. They are protons, neutrons, and electrons. Just by adding more protons for electrons, we get different elements. In principle, you can build a very simple universe with just protons, neutrons and electrons, but it became much more complicated in the beginning of the 20th century when we found many new particles from cosmic ray. There wasn't really a system es-

tablished to organize this zoo of particles, so we called those new particles with symbols, such as π, Σ, Δ, and so on. Things get so bad and we were running out of symbols to name those new particles, so we start to organize these particles according to the properties they have, such as electrical charge, spin, mass, and lifetime. To provide a simple picture, the new fundamental particles,quarks, was predicted. The whole zoo of particles could be described by a combination of these quarks. And this is the birth of standard model for particle physics.

There are six types of quarks, known as flavours: up (u), down (d), charm (c), strange (s), top (t) and bottom (b). The antiparticles of quarks are antiquarks. Quarks have various intrinsic properties, including electric charge, spin, mass and colour charge. In addition to this quarks, there is another set of the fundamental building of blocks in the model, known as leptons. They are electron, and its heavy cousins muon and tau, and their neutrino partners. A tipical standard model picture is shown as Fig1.1.

The standard model also incorporates with the fundamental forces. There are four way that things interact with others. There is gravity; if there is any mass at all, thing gets attracted. There is the
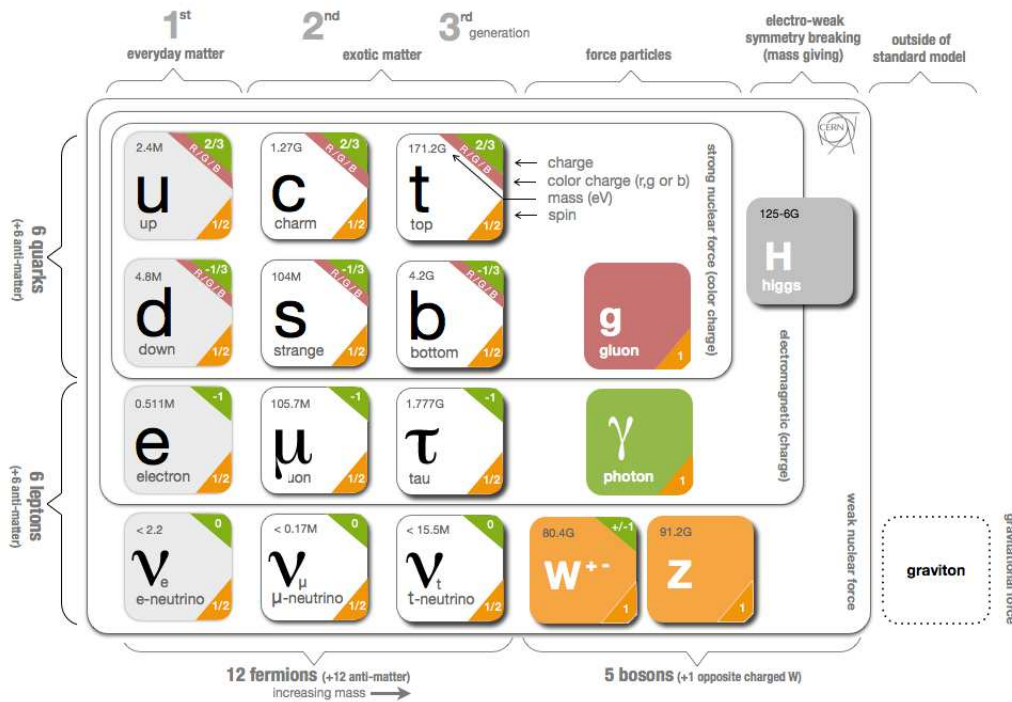
Figure 1.1: stardard model[2]

electromagnetic force which makes two charge repeling each other,
and that is a major force that you actually feel. The exchange par-
ticle for the electro-magnetism is the photon. There is another force
called weak force, which is similar with electrostatic forces but much
weaker. The exchange particles of weak interaction are W and Z
bosons. The weak force explains the energy production in the sun
and is responsible for the radioactive beta decay. There is a fourth
force called strong force. The exchange particle of the strong force
is gluon. The gluon literally glues together the quarks in the neu-

trons and the protons and hold nuclear together. The last piece of the standard model, Higgs, was discovered at LHC at 2012.

In the stardard model, a hadron means a particle which is composed of quarks. The quarks representing the explict quantum numbers of a hadron are valence quarks; There are two kinds of hadrons. The baryon is a hadron made with three valence quarks such as proton or neutron. The meson is a hardron which made with two valence quraks, such as pion,J/Ψ or Ψ'.

1.2 QCD

The "Parton" was proposed by Richard Feynman in 1969 as a generic description for any particle constituent within the proton, neutron and other hadrons. These particles are referred today as quarks and gluons. The theory that describes strong interactions is called Quantum Chromodynamics (QCD). QCD is very important in hadron collisions because the constituents of hadrons are partons. The three-quark model assuming that a proton or a neutron is made of three free non-interacting quarks in a bag is too simple. It cannot match a scattering process like the inelastic scattering of
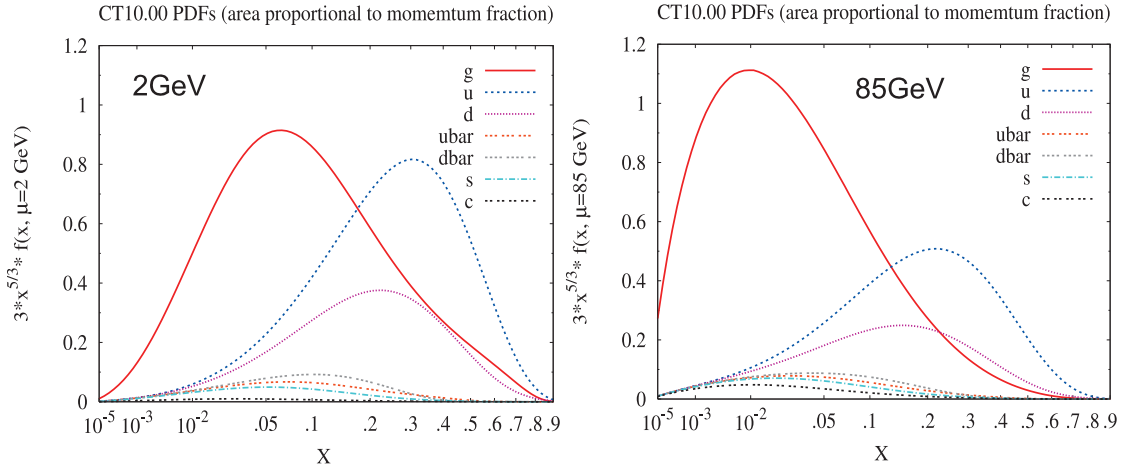
Figure 1.2: The example of the PDF function at Q=2 GeV and Q=85 GeVfrom the CT10 group[9].

electrons off protons. Those valence quarks are embedded in a sea of virtual quark-antiquark pairs generated by the gluons which hold the quarks together in the proton. All of these particles - valence quarks, sea quarks and gluons- are partons.

The number densities of the partons in the proton depend on the probing energy scale which is the virtuality of the incident photon, Q^2, and fractional momentum of the parton, x, with respect to the momentum of the proton, expressed by a parton distribution function (PDF), $f_i(x, Q^2)$, for each parton i. The PDF represents the probability densities (strictly speaking number densities) to find a parton carrying a momentum fraction x at a squared energy scale

$Q^2 = -q^2$. DIS experiments have shown that the number of partons goes up at low x with Q^2 , and falls at high x . At low Q^2 the three valence quarks become more and more dominant in the nucleon. At high Q^2 there are more and more quark-antiquark pairs which carry a low momentum fraction x . They constitute the sea quarks. A salient finding of the DIS experiments is that the quarks and antiquarks only carry about half of the nucleon momentum, the remainder being carried by the gluons. The fraction carried by gluons increases with increasing Q^2. While proton structure functions have been measured with deep inelastic scattering over five orders of magnitude in both the, x and Q^2, the factorizable, non-perturbative parton distributions must be determined by phenomenological fits[3, 4, 5, 6, 7, 8]. Perturbative QCD quantitatively describes the Q^2 evolution of the parton distributions, but the origins of the parton distributions themselves have not proved amenable to QCD treatment, although many models exist in the literature. Measurements of those distributions that are poorly determined provide vital information on nucleon structure which is used to constrain and refine the phenomenology.[1] The example of the PDF function at 2 GeV and at 85 Gev from the CT10 group

are shown as Fig1.2[9].

1.3   Deep-Inelastic Scattering (DIS) and Drell-Yan Process

The internal structure of the nucleons determines their fundamental properties, which directly affect the properties of the nuclei. Understanding how the nucleon is built by quark and gluon is one of the most important syudies in nuclear physics. The structure of the nucleon can be studied by scattering leptons, such as electron or muon, in a similar way that the structure of condensed matter or atoms can be studied through the scattering of X-rays, neutrons, and electrons. There are two reasons why the electromagnetic interaction is a good tool for taking a "picture" of the nucleon. First, QED is a "known" interaction. Second, perturbation theory is valid. We have a well-defined interaction for our probe and a systematic calculational scheme for computing the results of experiments. Electrons and muons can easily be accelerated in well-defined monoenergetic beams and accurately detected using magnetic spectrometers and standard particle detection techniques. There are two types of scat-

tering which are most useful in studying the nucleon. First is elastic scattering in which the final state of the nucleon remains the same. The scattering cross section could map out the charge and density distributions inside the nucleon, such as Rutherford scattering. Another one is the deep-inelastic scattering (DIS) in which a quark in a nucleon gets knocked out by the virtual photon, and the proton gets smashed into many hadrons. This process could extract the quark and gluon distributions in momentum space or parton distributions. However, there is another method, which is very similar to the DIS method, that is the Drell-Yan process[10]. The Drell-Yen process simply turns the DIS Feynman diagram for 90 degrees, as shown as Fig1.3. A quark of one hadron and an antiquark of another hadron annihilate into a virtual photon. The virtual photon decays into a pair of oppositely-charged leptons. This process was first suggested by Sidney Drell and Tung-Mow Yan in 1970[3] to describe the production of lepton–antilepton pairs in high-energy hadron collisions. A measurement of the tracks and momentum of charged particles from Drell-Yan could provide the mass and momentum of the vertual photon which helps to understand the PDF.
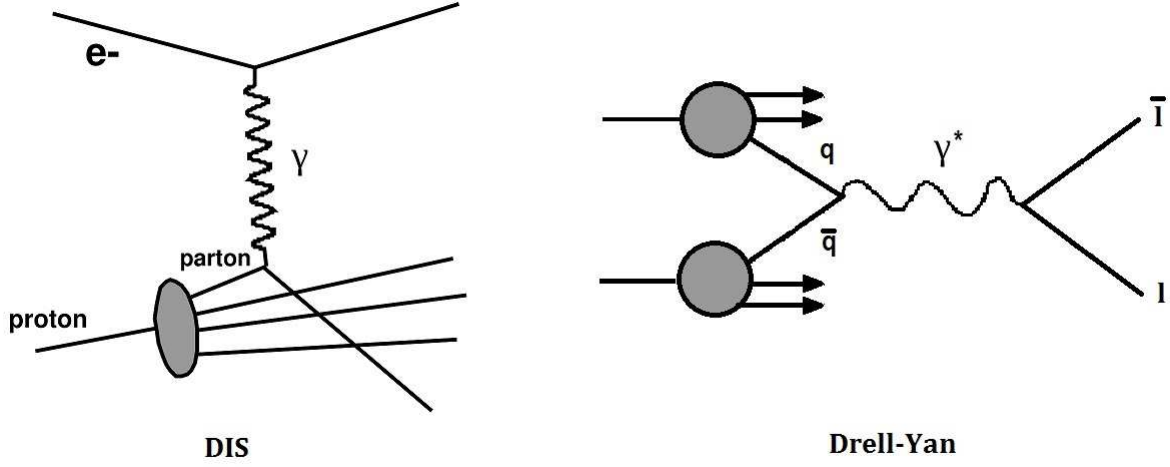
Figure 1.3: DIS and Drell-Yan

1.4   SeaQuest experiment

The SeaQuest experiment was designed for Drell-Yan process, and

measure the dimuon pairs. The features of the cross section were

explained in terms of 2 the parton model as a hard scattering of

point-like particles multiplied by a convolution of the parton distri-

butions of the interacting hadrons as the Eq.1.1.

$$\frac{d^2\sigma}{dx_b dx_t} = \frac{4\pi\alpha_e}{9x_b x_t}\frac{1}{s}\sum_i e^2\left[\bar{q}_{i \cdot target}(x_{i \cdot t})q_{i \cdot beam}(x_{i \cdot b}) + q_{i \cdot target}(x_{i \cdot t})\bar{q}_{i \cdot beam}(x_{i \cdot b})\right]$$

$$(1.1)$$

Where $q_i(x_i)$ is the parton distribution of quark with flavor i; e is
the charge of quark with flavor i; $\sqrt{s}$ is the center-of-mass energy;
α_e 1is the fine structure constant; and the sum is over all quark
flavors; $x_{i \cdot b}$ is Bjorken-x_{beam} of parton i; the $x_{i \cdot t}$ is Bjorken-x_{target}
of .quark with flavor i. According the Monte-Carlo, we can see the
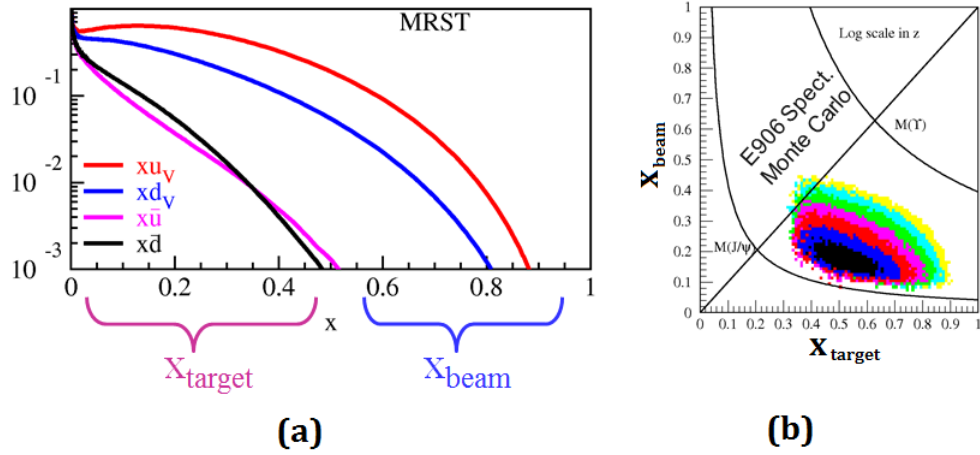
Figure 1.4: SeaQuest Acceptance

acceptance at at low x_{beam} and high x_{target}, so that the second term at Eq.1.1 is very low, so taht the SeaQuest mostly getting sea-quark from the target and mostly get the quark from beam proton.

1.5   J/Ψ and Ψ' production

The major background of the high-mass Drell-Yan process is from the charmoniums $(c\bar{c})$, more specifically, from J/Ψ and Ψ'. The charmoniums come from the quark-antiquark annihilation and gluon-gluon fusion. The charmonia production diagram from quark-antiquark annihilation and gluon-gluon fusion are shown as Fig. 1.5[31]

Charmonia production diagram from gloun-gloun fusion

Charmonia production diagram
from quark antiquark annihilation
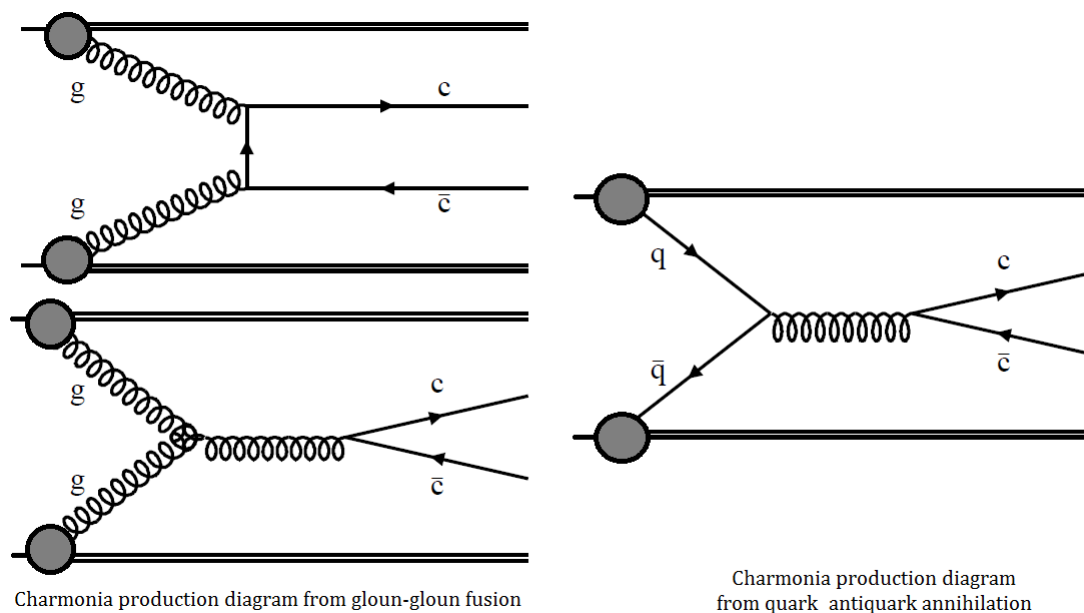
Figure 1.5: The charmonia production diagram from quark-antiquark annihilation and gluon-gluon fusion.

1.6   Other interesting physics

The observation of J/Ψ suppression is a signature of quark-gluon-plasma formation. Matsui's paper[14, 15] concluded that there appears to be no mechanism for J/Ψ suppression in nuclear collisions except the formation of deconfining plasma, and if quark gluon plasma is produced, there seems to be no way to avoid J/Ψ suppression [16, 17, 18, 19]. For instance, in the ref[21, 20, 22] studys, the nuclear modification factor has the p_T suppression, which is a sign of QGP. However, an observation of suppression alone does not prove that a plasma was created. For instance, the E886 experiment at

Fermilab found J/Ψ suppression in the cold nuclear medium, the detail of this will be described in the last section of the chapter. Other possible suppression mechanisms need to be checked to determine whether they can also produce a similar p_T-dependent suppression pattern. The earlier data on J/Ψ production in proton–nucleus interactions, showed that J/Ψ production is reduced in large nuclei relative to a proton target[18, 19]. Thus, the nuclear dependence, A-dependence, of J/Ψ production is less than linear, $\sigma_{pA} = A^\alpha \sigma_{pp}$ with $\alpha < 1$.

1.7 Production mechanism

Anothr interesting thing is the production mechanism of J/Ψ and Ψ'.

The cross sections of 2→2 QCD hard interactions ($q\bar{q} \rightarrow c\bar{c}$, $gg \rightarrow c\bar{c}$) do depend mostly on mass of J/Ψ and Ψ'. The collision energy does not play a role here[23]. However, the J/Ψ yield is the convolution of 2→2 cross sections and the parton density of $q(x)$,$\bar{q}(x)$ and $g(x)$. Since x=M(J/Ψ)/sqrt(s), the contributing x region

becomes smaller at larger collision energy and g(x) becomes strongly dominating at small-x. That is the reason why we speculate that $q\bar{q}$ might likely get even with gluon-gluon at low collision energies, for example, the collision energy at E906.

1.7.1   Initial-state and final-state effects

The beam parton moves across the target nuclei, then has a hard collision with the target parton.The initial and final states of the parton are marked before and after the happening of a hard collision. For the Drell-Yan process, the beam parton is one of the valence quarks, and the target parton is one of the sea quarks (anti-quark). After the hard collision, the quark and anti-quark annihilated to a virtual photon, then become a dimuon pair. The dimuon pair hardly has any interaction with nuclear medium, so that only initail-state effect is associated with the Drell-Yan process. For the initial state, there are a few source of p_T: the intrinsic p_T of inital state parton, single or multiple elastic scattering of initial state parton, gluon emission from initial state parton. rom

In high energy hadron-nucleus and nucleus-nucleus collisions, the

final-state effect and the initial-state effect can both change the heavy quarkonium's production rate and its momentum spectrum. The effect of the final-state interaction depends on the hadronization mechanism—how a produced heavy quark pair becomes a bound quarkonium. For the J/Ψ and Ψ' process, after the hard collision, the virtual photon or gloun will form a $c\bar{c}$. From the $c\bar{c}$ to J/Ψ and Ψ' status, we called it pre-J/Ψ and pre-Ψ'. The initial state takes place at such a short time that it is unlikely to interfere with the dynamics of the nuclear medium which is effectively frozen. On the other hand, the hadronization from the heavy quark pair to a bound quarkonium (final state) could be very sensitive to the medium properties. In this study we will use the Drell-Yan process as a controlled check, as we expect that compare with J/Ψ and Ψ' process, the Drell-Yan process will have much less interaction with nuclear medium.

A color-singlet heavy quark pair with a small color dipole moment is less likely to interact with the nuclear medium than a pair in a color-octet configuration [11, 12]. That is, the final-state effect could be an ideal probe for exploring the nonperturbative formation mechanism in heavy quarkonium production. But, the observed nu-

clear dependence is sensitive to not only the final-state effect but also the initial-state effect as well as the quantum interference between them. Because of the local hard collision that produces the heavy quark pair, the quantum interference between the final-state and initial-state partonic rescattering could be suppressed by the hard collision scale. To understand the effect of the initial-state interaction, we also study nuclear dependence in the production of the Drell- Yan virtual photon. The initial-state effect itself can be a good probe for the dynamics of partonic rescattering when a fast parton passes through the nuclear matter.[13]

1.8   J/Ψ and Ψ'

The radius of J/Ψ and Ψ' differ by a factor of 2[24, 25]. The larger the radius makes the larger corss-section. Because the radius of Ψ' is almost twice of J/Ψ, one would imagine that Ψ' should have much larger interaction with nuclear medium than J/Ψ and thus a stronger suppression of production in the nuclear medium. However, the story is more complicate than that. First, as Ψ' has higher

mass, and is the excited state of J/Ψ, Ψ' could decay to J/Ψ. In other words, when we found J/Ψ, it could decay from a Ψ' or a χ_c, which is a even higher excited state of $c\bar{c}$.

1.8.1   Nuclear effect

If there is no nuclear dependence, we can image that the cross-section of a proton hitting a carbon should be about 12 times of that a proton hitting a proton. We can write down Eq. 1.2.

$$\sigma_{pA} = A\sigma_{pN} \qquad (1.2)$$

However, if there exists a nuclear effect, we can see the Eq. 1.2 won't perfectly describe it, so that the Eq. 1.2 could be modified as Eq. 1.3.

$$\sigma_{pA} = A^{\alpha}\sigma_{pN} \qquad (1.3)$$

The α in Eq. 1.3 is presenting the nuclear dependence. If the $\alpha >$ 1 , it is called enhancement, which means the nuclear effect would increase the cross-section; if the $\alpha < 1$, it is called suppression,

which means that the nuclear dependence would decrease the cross section.

1.8.2   Kinematics

The E906 data may be divided into dierent kinematic regions in order to obtain a better understanding of the nuclear dependence. The kinematic variables that can be studied in E906 are mass, m; Feynman x, x_F; transverse momentum, P_T. Nuclear dependence has strong kinematic dependence; the x_{target} could provide information of EMC effect[27, 28]; the x_{beam} could provide information of energy loss[29]; the transverse momentum suppression in the cold nuclear medium could provide information of production mechanism of the J/Ψ and Ψ'.

1.9   What E772 and E866 found

The E772 has done nuclear dependence study of Drell-Yan process. The E772 used the following targets, LD2, carbon, iron ,and tungsten. The result is unpublished and can be found at E866

website[30], as shown as Fig1.6 . As only initail-state effect is associated with the Drell-Yan process, the ratios of different targets are close to one as expected. The E866 published the J/Ψ and Ψ' suppression[27, 26]. The result shown as Fig1.7. The substantial differences between J/Ψ and Ψ' production are observed for the first time in p-A collisionsst small p_T and small $x_F$region (SXF in the Fig1.7). Note that the E772 expriment was using LD2 as the reference target, but the E866 is using Beryllium as the reference target. The suppression for Ψ' production is stronger than that for J/Ψ for x_F near zero (SXF in the Fig1.7), but becomes comparable to that for J/Ψ for $x_F > 0.6$ (LXF in the Fig1.7). The E906 x_F is more close the LXF (large x_F, $0.3 < x_F < 0.93$) region of E866. As E866 found that the J/Ψ and Ψ' suppression is close in this region, the E906 runs at $E_{beam} = 800 GeV$ instead of E866 runned at $E_{beam} = 120 GeV$.
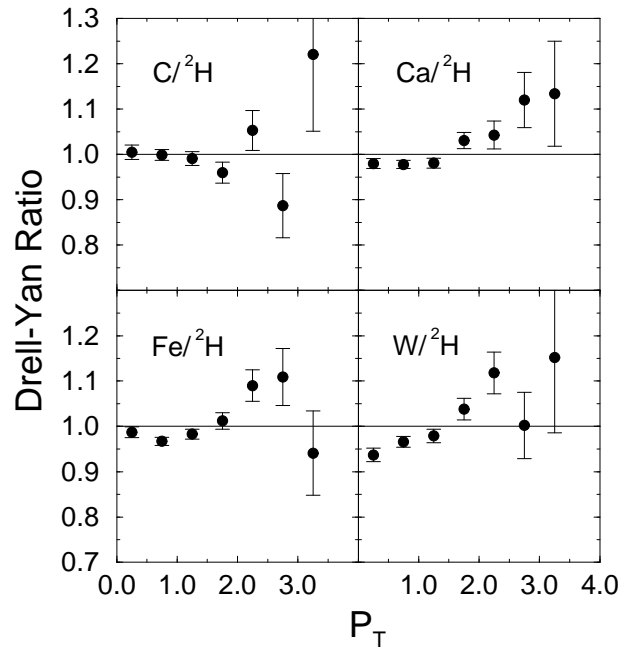
Figure 1.6: The E772 Drell-Yan Nuclear dependence ratio[30].
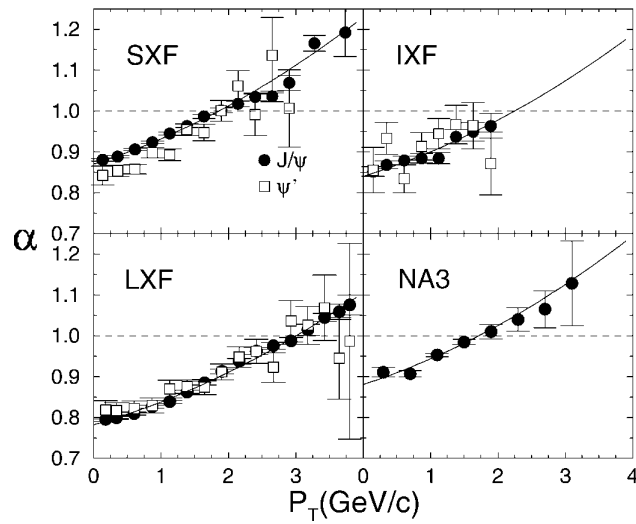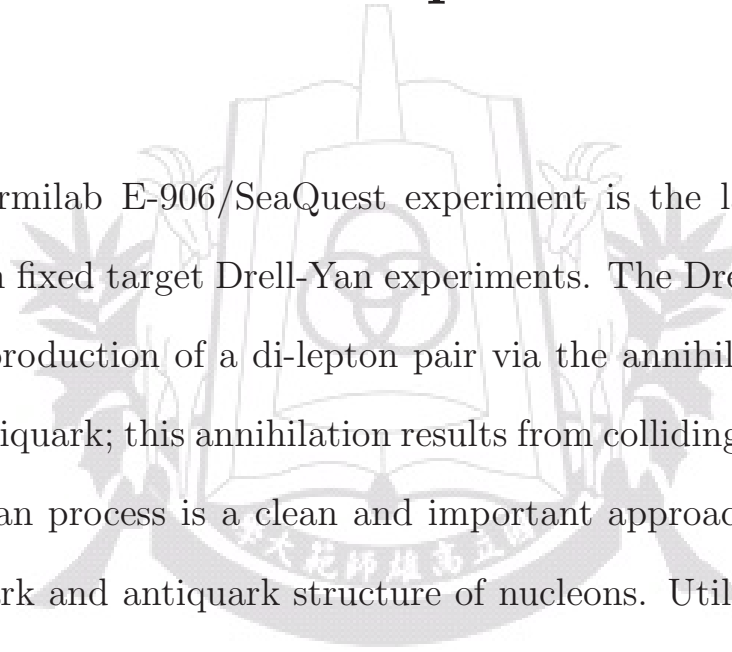
Figure 1.7: E866 result of nuclear dependence of J/Ψ and Ψ'[26].

Chapter 2

Experiment Setup

The Fermilab E-906/SeaQuest experiment is the latest one of a series in fixed target Drell-Yan experiments. The Drell-Yan process is the production of a di-lepton pair via the annihilation of quark and antiquark; this annihilation results from colliding hadrons. The Drell-Yan process is a clean and important approach to exploring the quark and antiquark structure of nucleons. Utilizing the high-intensity 120-GeV proton beam from the Main Injector at Fermilab, the SeaQuest experiment is able to determine both the antiquark structure of the nucleon in the large momentum-fraction region as well as the modifications of this structure inside the nucleus[1]. The detector system of this experiment is composed of drift chambers, proportional tubes, and scintillating hodoscopes. The drift time of
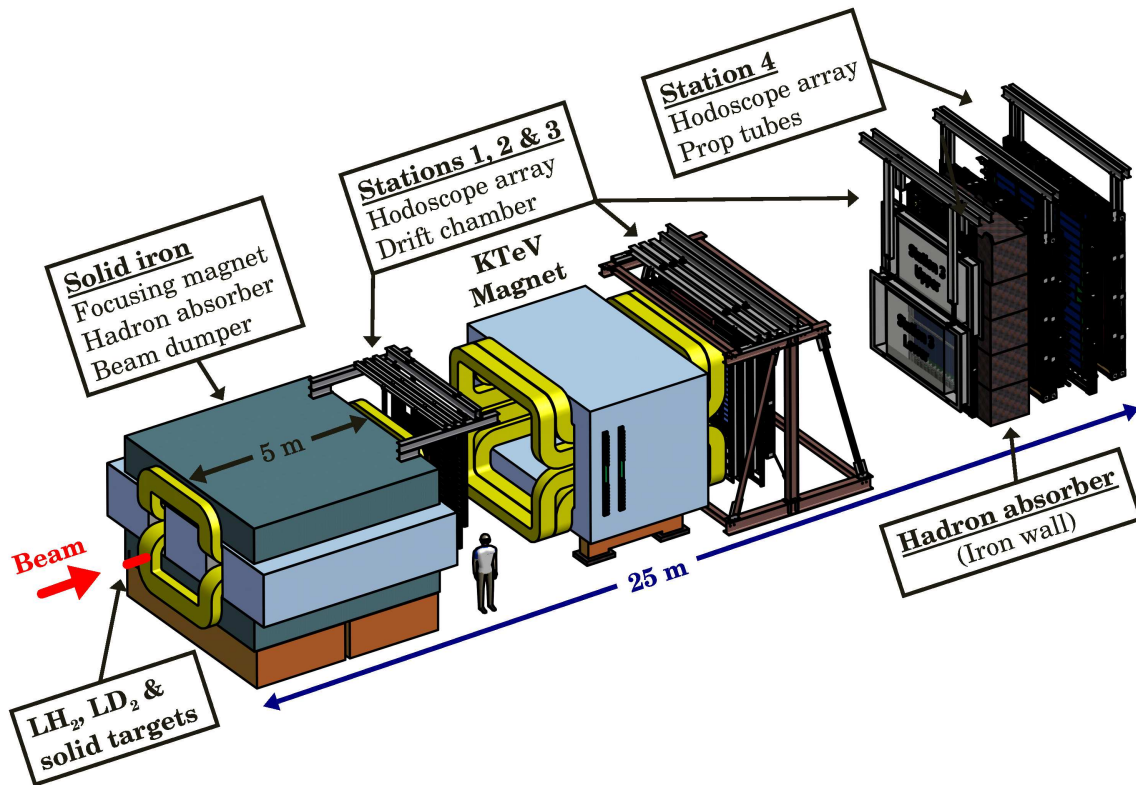
Figure 2.1: This figure schematically shows the SeaQuest spectrometer. The 120 GeV proton beam enters from the left, and the solid iron magnet also serves as an absorber for the beam that did not interact in a target.

the drift chambers and the proportional tubes indicate the position of the particle. The drift time information is digitized by time-to-digital converter (TDC) modules[45]. The detailed information of experiment setup could be found in the E906 sepctrometer paper, which will be submit in 2016. In this chapter, we describe the sepctrometer and introduce our DAQ system and electronics in more details[32].

2.1 Beam

SeaQuest uses a 120 GeV proton beam from the Fermilab Main Injector. The beam is extracted in a "slow spill" lasting just under four seconds. Typically, the time between spills is just over one minute. Beam is extracted using a resonant process and the extracted beam retains the 53.1 MHz structure of the Main Injector RF. Each bunch of protons is less than 2 ns long and the time between bunches is $\approx$ 18.8 ns. One can find more information about slow spill or slow extraction from Ref[62].

2.1.1 Trigger Sensitivity to Instantaneous Intensity

The SeaQuest beam is not uniform in time throughout the slow spill. The main reason of uniform is that is hard to control the portion of beam from QXR, or quadrupole extraction regulation system[62].

The SeaQuest Beam DAQ system can read out approximately 1000 events per second without significant dead time. During the commissioning of SeaQuest, the trigger rate was very high and the

trigger dead time was close to 100%. These triggers were taken at such high instantaneous luminosity that the occupancy of all SeaQuest detector elements was more than 50%, making pattern recognition essentially impossible. The Beam Intensity Monitor was designed to solve this problem.

2.1.2 Beam Intensity Monitor

The SeaQuest Beam Intensity Monitor (BIM) senses when the beam intensity is above a (programmable) threshold and inhibits triggers until the intensity falls to an acceptable level. Typically, the inhibit threshold is set at $\approx 95,000$ protons per RF bunch. The beam intensity is measured using an atmospheric pressure gas Čerenkov counter. The counter and readout electronics were designed to have good time resolution and a linear response over a large dynamic range. A diagram of the counter is shown in Fig. 2.2. A 45 degree aluminized Kapton mirror held on an elliptical G10 frame directs light to a single photomultiplier tube. A two-inch diameter 8-stage photomultiplier tube is positioned close to the mirror so that all Čerenkov light falls directly on the face of the phototube.
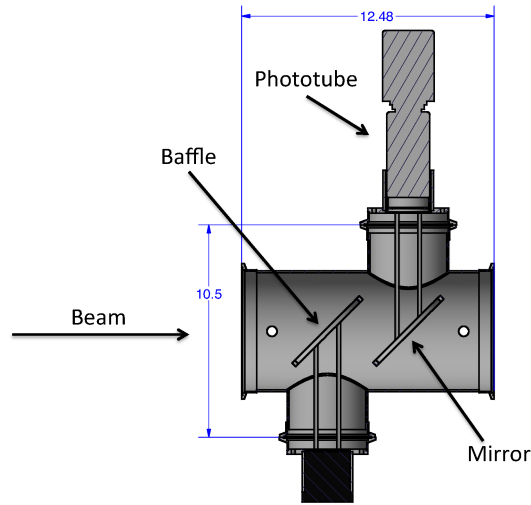
Figure 2.2: Beam Intensity Monitor

The BIM photomultiplier tube signal is integrated and digitized using a custom integrated circuit designed at Fermilab for CMS. This chip is one of the "QIE" family of circuits used first by the KTeV experiment at Fermilab[33]. QIE stands for Charge (Q) Integrator and Encoder. The chip is clocked with the Main Injector RF clock and provides an ADC conversion every RF clock. The QIE also recorded other informations, the details will be described in the Beam DAQ section.

Position	Material	Density[g/cm^3]	Thickness[cm]	Spill/Cycle
1	LH_2	0.071	50.8	10
2	Empty Flask			2
3	LD_2	0.163	50.8	5
4	No Tarrget			2
5	Iron	7.87	1.905	1
6	Carbon	1.80	3.322	2
7	Tungsten	19.30	0.953	1

Table 2.1: Target information.

2.2 Targets

The SeaQuest targets reside 50.8cm upstream of the face of the beam-dump/focusing magnet iron. The general design and many parts of the target are inherited from the E866/NuSea experiment. As depicted in Fig. 2.3 (left), the target system consists of two liquid targets, three solid targets, and two positions for measuring background count rates : an empty flask and an empty solid-target holder. The targets are mounted on a remotely positionable table which translates in a direction perpendicular to the beam axis over a range of 91.4cm. The details of the target materials in the seven target positions are summarized in the Table. 2.1.

Each of the three solid target positions is divided into three disks of 1/3; the total thickness provided in Table 2.1. These are spaced

25.4cm apart to approximate the distribution of the liquid target thereby minimizing target-dependent variation in spectrometer acceptance. The one exception to this is that during the Run2 period the iron plugs were more closely spaced (17.1cm).
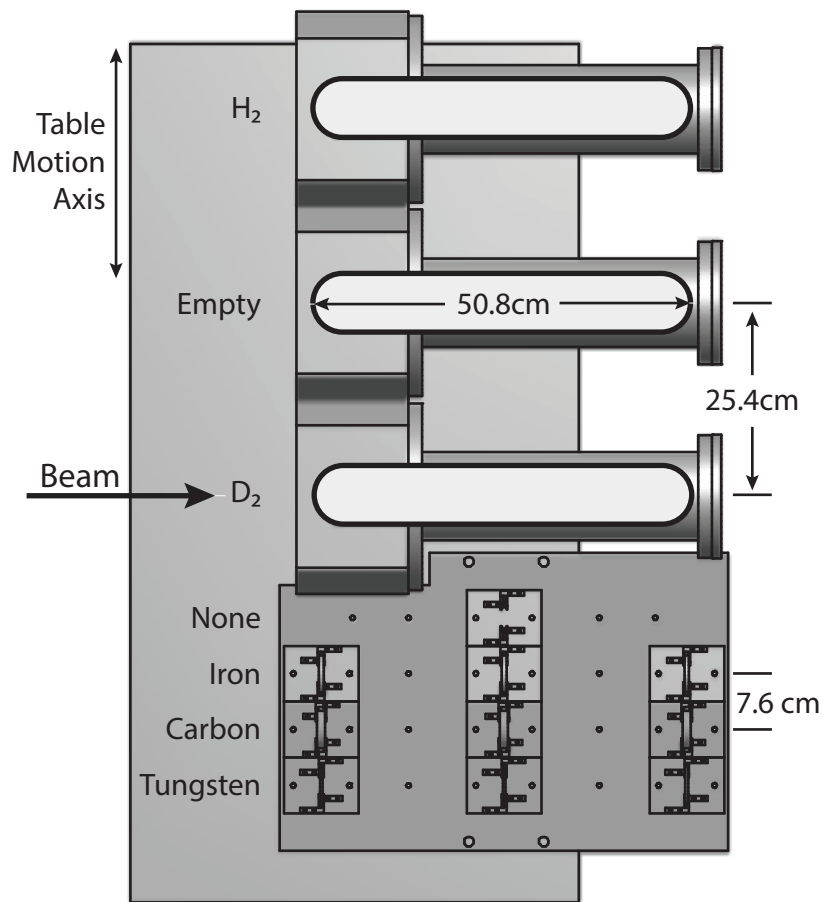
Figure 2.3: Layout of positionable target table showing the seven target positions.

2.2.1   Table Motion

Motion of the target table is accomplished with a stepper motor
driving a lead screw which moves the table itself on rails. The step-
per motor, motor driver, and motor controller are made by Ana-
heim Automation. The target positions are confirmed by monitor-
ing magnetic proximity switches mounted to the translating table
and platform base. The software step position is recalibrated to the
edge of the central proximity sensor each time the table passes.

2.3   Magnets

There are two large dipole magnets. The most upstream mag-
net, denoted FMag, is a solid iron A-frame magnet assembled from
43.2cm x 160cm x 503cm iron slabs, as shown in Fig. 2.4 The mag-
net has no air gap and the iron has extremely high purity, allowing
a 2000A excitation current to generate a central magnetic field of
1.9 Tesla (yielding a 2.8 GeV total magnetic deflection). FMag uses
one of the three sets of "bedstead" coils recovered from the disman-
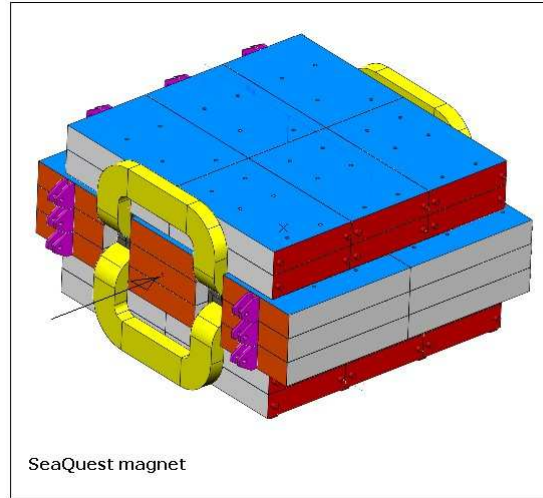
Figure 2.4: Perspective drawing of FMag showing the arrangement of the iron slabs.

tled E866 SM3 magnet [34, 35, 36, 37]. FMag also acts as the beam dump for the 120 GeV beam delivered to the SeaQuest spectrometer. There is a 5cm diameter by 25cm deep reentrant hole drilled into the upstream end of FMag. The 120 GeV protons in the beam, that do not interact in the SeaQuest targets 125cm upstream of FMag, interact in the central iron slab.

The downstream magnet, denoted KMAG, is a 300cm long iron rectangular magnet with a 289cm wide by 203cm high central air gap. It was originally constructed by the E799/KTeV collaboration at Fermilab. It is excited to a central field of 0.4 Tesla (0.41 GeV magnetic deflection) by 1600 Amps at 270 Volts (430kW).

2.4   Detectors

The detector system of this experiment is composed of drift chambers, proportional tubes, and scintillating hodoscopes. The drift time of the drift chambers and the proportional tubes indicate the position of the particle. There were four detector stations in the E906 spectrometer denoted as Station 1 to Station 3 each consisted of hodoscopes and drift chambers while Station 4 consisted of hodoscopes and proportional tubes. The drift time information is digitized by time-to-digital converter (TDC) modules.

2.4.1   Hodoscopes

There are hodoscope planes in each tracking station. These hodoscopes provide fast tracking signals for use in triggering. In Stations 1 and 2 there are two hodoscopes planes which measure the X and Y intercepts of the tracks. In station 3, there is only X hodoscope plane. In station 4 there are 1 X plane and 2 Y planes. Each hodoscope plane was arranged into two halfplanes of parallel scintillator paddles which were attached to photomultiplier tubes

via plexiglass light guides. The hodoscopes at station 1~3 have photomultiplier tubes attached to one side, and station 4 has photomultiplier tubes attached to both sides. All hodoscope signals go through the CAMAC discriminator then feeded to v1495 trigger matrix and TDC.

2.4.2 Tracking Chambers

Each of Stations 1, 2 and 3 is equipped with a drift chamber (DC) to measure the passing x and y positions of muons at its z location. The trajectory of muons is reconstructed with the measured positions, as described later. The DCs at Stations 1 and 2 are called "DC1" and "DC2", respectively. Two DCs at Station 3 cover the top and bottom halves, and are called "DC3p" and "DC3m" where "p" and "m" stand for "plus" and "minus".

The basic structure is common to all the chambers. Each DC consists of six planes of sense wires. Wires are aligned in the vertical direction in two planes called "X" and "X'". Wires are tilted by +14 degrees in other two planes called "U" and "U'", and by −14

Chamber	Plane	Number of wires	Cell width (cm)	Width × height (cm)	z-position (cm)
DC1.1	X	160	0.64	102 × 122	617
	U, V	201	0.64	101 × 122	±20
DC1.2	X	320	0.50	153 × 137	617
	U, V	384	0.50	153 × 137	±1.2
DC2	X	112	2.1	233 × 264	1347
	U, V	128	2.0	233 × 264	±25
DC3p	X	116	2.0	232 × 166	1931
	U, V	134	2.0	268 × 166	±6
DC3m.1	X	176	1.0	179 × 168	1879
	U, V	208	1.0	171 × 163	±19
DC3m.2	X	116	2.0	232 × 166	1895
	U, V	134	2.0	268 × 166	±6

Table 2.2: Parameters of all chambers. Those of primed planes are almost the same as of unprimed planes. The z-positions of U and V planes are relative to those of X planes. [32]

degrees in the other two planes called "V" and "V'". The wires in the primed planes are offset by half the drift cell size to resolve the left-right ambiguity of drift direction. Every wire plane is flat vertical to the z-axis, and a drift cell is of the box shape. Summaries of the parameters of the DCs, along with the upgrade of DC1 and DC3m during the data taking, as listed in Table. 2.2.

The gas mixture for DC1.2 is Argon:CF4:Isobutane:Methylal, with the ratio of (68%:16%:13%:3%). The drift velocity is greater than 50 μm/ns (i.e. fast gas) and thus the hit-rate tolerance is bet-

ter. The gas mixture for the other chambers is Argon:Methane:CF4 (88%:8%:4%).

2.4.3 Muon Identification

Station 4 was also called the muon station. It was located downstream of the calorimeters and consisted of three hodoscope planes XYY and two proportional tube planes. Each of the proportional tube plane has horizontal (H) and vertical (V) subplanes, which are P1H, P1V, P2H, P2V. The proportional tubes used the same gas mixture, Argon:Methane:CF4 (88%:8%:4%), as the drift chambers

2.5 Trigger

We use 5 commercial FPGA modules (CAEN V1495) as the trigger matrices and TDC modules. These are commercially available 6U VMEbus modules featuring an Altera EP1C20F400C6 FPGA. Custom firmware has been written to meet the requirements for the SeaQuest trigger. The FPGA receives up to 96-channel inputs

and digitizes the leading edge time at 1 ns resolution using TDC blocks in the firmware. Digital processes on the outputs of the TDC include adjusting delay channel-by-channel in 1-ns steps, setting coincidence range and re-align with the accelerator bucket clock. The re-aligned hits are further processed in trigger matrices. SeaQuest uses four scintillating hodoscopes and a 4-out-of-4 majority coincidence logic is used to generate valid track information as trigger primitives to form a final global trigger. Zero-suppressed TDC data are read out for each event and the module could be used as a 96-channel TDC[38]. Four level 1 Trigger modules receive the Hodoscope signals. If any of them fire the single muon road, it will output a signal. The signal may go to different outputs of Level 1 Trigger module according to the charge and momentum of the single muon. The level 2 Trigger module then collects the Level 1 outputs from four different level 1 trigger modules. If the level 2 trigger module decides to fire the trigger, it will output a trigger from the outputs. There are up to 5 outputs of level 2 trigger module.

All levels of Trigger module has the ability to output the TDC value for main CODA to readout.

Other than the physics trigger (FPGA1), we also have special
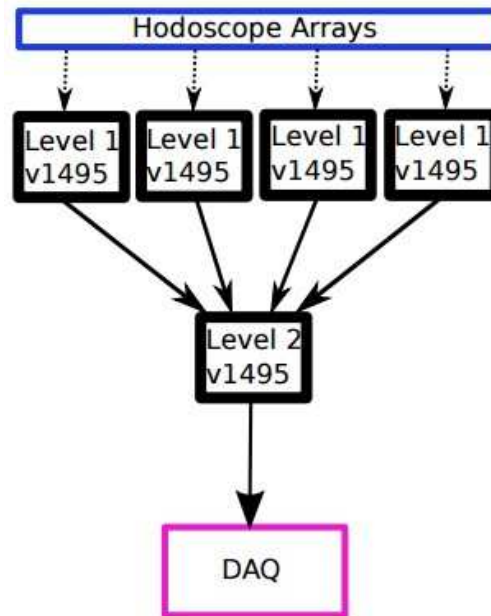
Figure 2.5: trigger matrix

triggers. All triggers are listed at table1.

2.6 Front End Electronics (FFEs) for DAQ system

Most of SeaQuest FFEs comply with the form factor of VME 6U standard for the mechanical specifications, except the Trigger supervisor (VME 9U) and QIE (NIM). The Time-to-Digital Converters (TDCs) is next section by its own as it is the major electronics and

name	function
FPGA1	Physics trigger (TB/BT)
FPGA2	both muons (TT/BB)
FPGA3	like-sign trigger (TB/BT)
FPGA4	single-muon trigger (T)
FPGA5	single-muon trigger (B)
NIM1	$st1X \oplus st2X \oplus st3X \oplus st4X$
NIM2	$st1Y \oplus st2Y \oplus st4Y1 \oplus st4Y2$
NIM3	Random RF
NIM4	cosmic
NIM5	flash events
BOS	begin of spill
EOS	end of spill

Table 2.3: Triggers for Main DAQ

has long history.

2.6.1   ASDQ and Level Shift Board (LSB)

The SeaQuest wire chamber readout system uses a custom amplier-364 discriminator integrated circuit called ASDQ designed at U. Penn. for CDF[39]. 8-channel ASDQ cards are mounted on each wire chamber. A single twisted pair ribbon cable connects each ASDQ card to a LSB. Each LSB services 8 ASDQ cards. Up to 14 LSBs are housed in a 9U crate. The LSB converts the dierential signals from the ASDQs to standard LVDS (Low-voltage differential signaling). The LVDS outputs are carried on 4 ribbon cables to

TDC. The details of TDC will be discribed at next section.

2.6.2 Trigger Supervisor (TS) and Trigger interrupt (TIR)

The TS provides the handshake between the logic trigger and Main DAQ. The TIR provide the handshake between the TS and each ROC. When the Trigger is accepted, the TIR also send the interrupt to each ROC, so that each ROC can read out front end electronic individually[40, 41].

2.6.3 SIS3610

The SIS3610 provides the handshake between the logic trigger and Scaler DAQ and sends the interrupt to the ROC when the scaler DAQ accepts the trigger[42].

2.6.4   Charge Integrator and Encoder (QIE)

The QIE connects to both BeamDAQ and MainDAQ. The detail of this electronic can be also found in the Beam section

The QIE is a custom-made chip that contain the charge-integrating electronics with an analog-to-digital converter (ADC). The input of QIE is beam Cerenkov counter which record how many proton we received. The trigger used for this system will also be the RF clock coming from the accelerator, which means we will receive a bucket by bucket measure of the beam intensity. QIE retains all 53MHz x 5sec data in its buffer for fast readout all this while keeping track of a running sum of *intensity*. BeamDAQ readout this information once a spill (one minute) through the internet ports.

QIE also receive a trigger from mainDAQ. Once the mainDAQ accept a trigger, TS will send a trigger to QIE, which will trigger QIE to send data to SL (see next FFE module). BeamDAQ also saves this information to an ASCII file.

If the beam intensity in RF buckets neighboring the trigger is deemed too high, then the board will issue a veto signal to the strobe-coincidence. All physics triggers go through strobe-coincidence

(LRS370)[43] to the TS so that the MainDAQ won't take physics trigger when beam intensity is higher than the user-selected threshold.

2.6.5 Scaler

The VME Scaler used for this system is a custom made 32bit-per-channel 140MHz scaler produced by IPN Orsay for the G0 Experiment at JLab[44].

2.7 Time-to-Digital Converters (TDCs)

The analog signals of the energy loss of charged particles in the detectors are digitized with time-to-digital converter (TDC) modules. This module was designed to be flixable for the degital signal readout.

2.7.1   Hardware Specification

This 64-channel module has 6U VMEbus form factor and is equipped with a low-power and radiation-hardened Microsemi ProASIC3 Flash-based FPGA. There are one internet port, one console port, a 20 pin ECL/LVDS port at front panel, and 3 limo ports located at front panel. There is also a USB port locate at the side of the board. The low-voltage power supply was +5.0 V and -12 V, provided by the VME backplane. The PCB was made of the FR-4 material with 1.6 mm thickness and double side assembly. An 8-layer PCB was used so that the front-end circuit had a better capability of EMI rejection. With the current Run2-TDC firmware, the power consumption for the whole module during standby was 0.86 A for +5V, and 4.7 mA for -12V. The input section contained 16 LVDS transceivers (Texas Instruments, SN65LVDT348) to interface with the differential digital signals from the front-end electronics. The transceiver chip could handle a variety of differential and single-ended logic levels (e.g. ECL, LVDS, LVECL, and PECL as the input and provides Low-voltage TTL (LVTTL) for the output logic). Each transceiver channel was integrated with an 110-ohm line termination resistor to

match impedance with the twisted-pair flat cable (3M, 1700 series). The buffer received differential signals from the cable and transmits them to signal-end FPGA inputs (Actel, A3P1000). The DAQ system read the buffer, which had the digitized TDC information though the VME backplane. In addition, we paid special attention to the layout to ensure that the trace lengths (or propagation delay) between the LVDS buffer and FPGA were no more than 1 mm in order to minimize the jittering of arrival time.

The core chip in this TDC module was the Actel ProASIC3 FPGA (A3P1000) [8], which was the most advanced device in the ProASIC3 series. It was also low-power and radiation-hardened. The main features of this FPGA device were as follows: 1 M system gates, 144 kbits dual-port SRAM, one integrated PLL, 300 user-defined I/O pins, and 350 MHz system performance. This on-board FPGA was incorporated with three major off-chip silicon resources: the 64-channel front-end transceivers, memory chips (IDT, 32K x 16-bit, IDT70V27), and interfaced with the 32-bit VME backplane. To relieve the bandwidth bottleneck of these circuits, a large portion of pin count was used in the FPGA to provide most of the throughput advantage. The LVTTL logic was selected for all FPGA I/O

buffers, and the drive current was limited to 6 mA for a better quality of signal integrity.

For the development of the FPGA firmware, Libero IDE 9 design software was used for the synthesis, simulation, and timing analysis. The binary design file was downloaded to the flash-based FPGA by connecting the FlashPro4 programmer to the on-board JTAG port.

The system clock source was a flash-programmable clock generator (Cypress, CY22394). It was the output clock used for the real-time clock (RTC), Ethernet synchronization, and a differential LVPECL clock for the PLL inside the FPGA. The PLL was locked to a reference 135 MHz LVPECL clock source, which provided a low jittering peak-to-peak performance of 200 ps.

For the future upgrade, this module also comes with an Arm processor which allow users to install a kernel or Linux system, and to buffer the data in the memory chips and readout from the internet port from the front panel.

2.7.2 Design and History

This hardware design allows users to put the different logic into the FPGA code. In SeaQuest experiment, this module is not only used as a TDC card, it is also used as a Scaler-Latch (SL) card with different firmware.

Originally, a latch-type FPGA firmware was used for the TDC function, and the time resolution was 2.5 ns. Since there was no great need for gate elements and high speed in the latch-card design, Actel ProASIC3 FPGA (A3P1000) was chosen. This FPGA was the most advanced device among the ProASIC3 series. The Actel flash-based FPGAs have low power consumption and are radiation-hardened for the single-event-effect (SEE). The Flash configuration cell is sensitive to total-ionizing-dose (TID) effects. In x-rays the TID limit of this sub-circuit is between 40 and 50 Krad. According to our estimation, in the E906 experiment, the total radiation for a two-year run is less than 0.1 Krad [9]. However, the flash-based FPGA has no dedicated carry lines, and the shortest delay time through a logic block is hundreds of picoseconds. Thus, it needs more effort to improve the time resolution [10, 11, 12].

Due to the lack of zero suppression, the large data size caused significant DAQ deadtime. During the one-year shutdown between Run1 and Run2, we decided to make another FPGA firmware (Run2-TDC) with zero-suppression and 0.444 ns resolution using the same hardware, so that the data volume and the data acquisition (DAQ) deadtime could be reduced. Even though the experimental requirement of time resolution was 4 ns, a better time resolution provides more information, especially during the commission stage when the trigger and electronic system was intensively debugged and cross-checked. On the other hand, E906 was still developing one more chamber, which needed better resolution. Thus, we made a TDC firmware with a better resolution than Run1-TDC with current hardware.

The design of new FPGA firmware (Run2-TDC) aims to reduce the data volume and data acquisition (DAQ) deadtime. The firmware digitizes multiple input hits of both polarities while allowing users to turn on a multiple-hit elimination logic, which removes after-pulses in the wire chambers and proportional tubes. A scaler is implemented in the firmware to record the number of hits in each channel.

2.7.3 TDC Firmware Overview

The block diagram of the Run2-TDC firmware is shown in Fig. 2.6. There are two common methods for a delay chain: logic elements delay and carry chain delay. The logic elements delay was tested in the early design. However, it was coarser than the carry chain delay, and we decided to use the carry chain method. The 9-tap delay line was implemented with 9 VersaTiles as shown in the left most block ("Delay9ph," in Fig. 1(b)). The VersaTiles for the delay elements were placed together in a chain to achieve the shortest and uniform propagation delays, which could be considered fixed for a particular physical technology, rail voltage [52]. The VersaTiles used as D-flip-flops were placed next to the delay chain for most uniform propagation delays. The input hit in each channel propagated in a delay chain [53] of 9 taps with a nominal delay of 450 ps/tap. The delay pattern was registered at every clock cycle at 250 MHz and was encoded into the fine-time code. If a valid hit was detected, the fine-time code (a hexadecimal value from 0 to 8) along with the coarse-time count (with a least significant bit equal to 4 ns) were temporarily stored in the first-layer buffer (Pipe4) with up to 4 hits
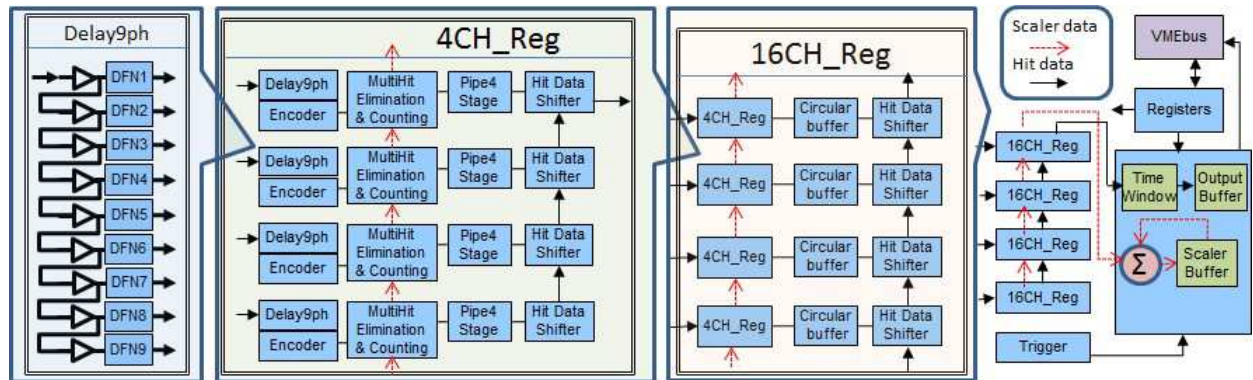
Figure 2.6: Block diagram of the TDC firmware.

per channel. The stored hits were constantly read out at the speed of 62.5 MHz and were put into a block of memory shared by a group of 4 channels.

The memory was organized as 2, 4, or 8 pipelines (circular buffers) with a user-select length of 2048, 1024 or 512 ns to store hits waiting for the trigger selection. If a trigger arrived, the writing pointer was directed to the address of the next circular buffer and the current circular buffer was read out by copying valid hits into the event buffer. During the read out time or copy in progress (CIP) time, the TDC was only allowed to record hits within a preset time window to accommodate various detectors with different sizes and drift time. The TDC data of hits stored in the event buffer were read out by the DAQ system via the VMEbus interface.

2.7.4 Coarse-Time Counter (TC) Implementation

The key to reduce the need of resource is the Coarse-Time Counter inplementation. The ProASIC3 flash based FPGA family is relatively slow in terms of clock speed. A frequency of 250 MHz for the delay pattern register clock was used to reduce the delay line length and the encoder size so that 64 channels could be fitted into a low-cost device. However, as many authors in this field have pointed out, it is very difficult to implement other logic blocks at the same 250 MHz, especially the coarse-time counter.

To overcome this problem, we implemented the higher bits of the coarse-time counter, TC[2-10] with 62.5 MHz, and the lowest two bits of it, TC[0-1] with 250 MHz, as illustrated in Fig. 2.7. To synchronize the lowest two bits of the coarse-time counter, a 4 ns pulse was used to reset the counter running at 250 MHz. The reset pulse was made by an AND gate and three D-flip-flops (DF) in the 250 MHz clock domain. The first flip-flop (DF0) caught the rising edge from TC[2], which fliped every 16 ns. The second flip-flop (DF1) caught output from the DF0 so it was two clocks later in comparison with TC[2]. The inputs of the AND gate were DF0 and
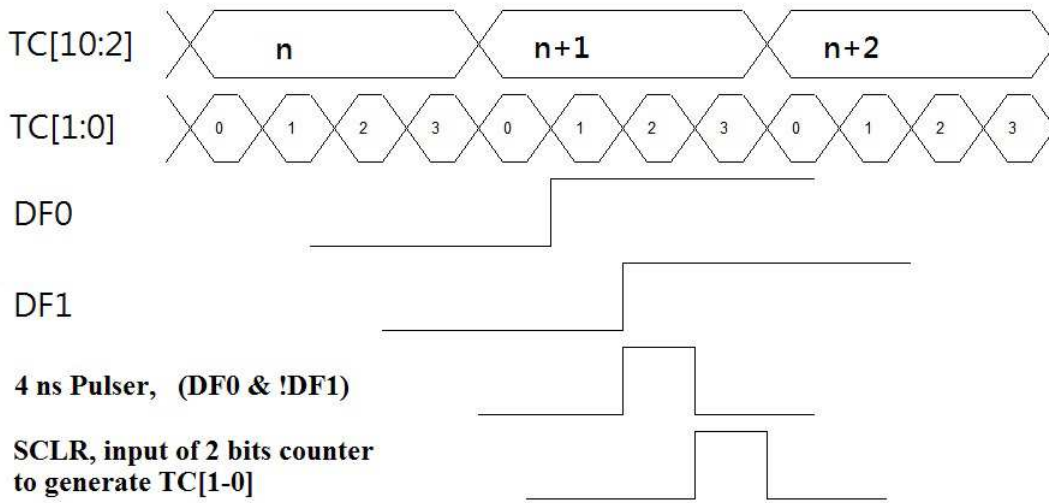
Figure 2.7: Coarse-time counter implementation

the inverse of DF1. The output of the AND gate went to the third flip-flop, and its output (SCLR) was used as a synchronous reset signal of the two-bit counter TC[0-1]. In this way, only two bits of the coarse-time counter were running with a 250 MHz clock.

2.7.5   Scaler

In almost all applications, it is highly desirable to implement a scaler for each TDC channel as a tool for deadtime estimation or quick detector checking. The conventional method of implementing a scaler consumes a large amount of FPGA silicon resource. Therefore it

is difficult to pair a scaler with each TDC channel. We made an innovation by developing a new scheme with reduced resource consumption that allowed us to fit 64 scalers with the 64 channels. The resolution of each scaler was 16 ns, and there was an 8-bit counter for each channel.

These counters were synchronously read into the first-layer buffer and then reset. The 64 first-layer buffers then passed scaler data one at a time, taking 2048 ns in total to read out all channels. Within this 2048 ns time period, a channel could receive a maximum of 128 hits without the overrolling of the 8-bit counter. In the final buffer stage, a 32-bit adder was used to accumulate the output from the 8-bit counter for each channel and to store the value into a 32-bit buffer so that the scaler could count up to 2^{32}. The buffer was organized as 8 pages with 64 channels for each page. The user could switch to a specific scaler page by setting an accessible register via the VMEbus.

2.7.6 Scaler-Latch (SL)

The SL is using the same hardware with TDCs. The only difference is the firmware. The SL receives the 16 channels ECL output from QIE. The initialization of SL is that all 16 channels are low for longer than 12.8 μs. The trigger of SL is when SL gets a non-zero signal, then every 100ns, SL record 16 bits data until the 128 words are captured for each trigger. If there are more than 128 words, the extra word will start a new trigger, and overwrite the buffer. The acceptable range for a single input period is 100±0.5ns.

The SL readout the ECL signal every 100 ns, and record the "channel to bit result" for 16 bits. For instance, it records channel 0 high as bit 0 equals 1, channel 1 high as bit 1 equals 1, channel 2 low as bit 2 equals 0.

The information that QIE pass to SL is the spill counter, time stamp, ADC value of 33 RF buckets (the triggered RF bucket and +-16 RF buckets). The spill counter here added up with the spillID of all DAQ.

2.8 DAQ

Data acquisition for the detector requires a bandwidth and different timing which cannot be provided by a single central computer system. The SeaQuest has three DAQ subsystems. They are Main DAQ, Scaler DAQ, and Beam Cerenkov DAQ. The Main DAQ records the main detector information and the trigger timing. The Scaler DAQ records the scaler information once per spill to study the main DAQ dead time. The Beam Cerenkov DAQ records the information from the QIE (charge integrator encoder) board that is programmed to encode the amount of charge accumulated through its input at the RF frequency.

The spectrometer includes four detector stations, each with a set of hodoscope (scintillator) plane and a set of wire chamber (station 1-3)/proportional tube. The hodoscopes are designed to provide the stop trigger for the Main DAQ system while the chambers and proportional tubes give the position and timing of the muons as they pass through the stations. The timing of the muons is recorded as the signals from both the hodoscopes and the chambers are connected to time-to-digital convertors (TDC). There are 89 TDCs

being used to read out the 4 detector stations. The TDCs receive two types of signals for which their arrival times are recorded; the chamber, proportional tubes and hodoscope signals, and the stop trigger. Since the stop trigger is common to all of the TDCs, it provides a reference against which the chamber and hodoscope arrival times can be compared. All the signal arrival time, and thus the time when the particles hit, for each detector can be compared to each other via this reference.

The signals from the hodoscopes go to three different destinations. One is the TDCs, where the timing of the hodoscope hits is recorded with respect to the stop trigger. The hodoscope signals are also sent to a set of NIM electronics where a set of simple coincidence triggers is created. These are used primarily for special purpose runs and to debug/understand our spectrometer. The third destination of the hodoscope signals is the FPGA trigger matrix, consisting of nine v1495 VME FPGA boards. The main purpose of these FPGA boards is to create a more sophisticated trigger that involves not only the coincidence of the four detector stations, but also cuts to make sure that the dimuon candidates took the correct flight path, or "roads", as determined by Monte Carlo simulations.

The FPGA logic is performed in three stages. In the Level 0 trigger, consisting of four v1495 boards for the four stations, the time of the signal is recorded in a manner similar to the TDCs (v1495-TDC). This allows us to monitor the FPGA logic to make sure that the dimuon triggers produced by downstream logic were indeed correct or not. In the Level 1 trigger, consisting of another four v1495 boards, the position and timing of the hits from each hodoscope plane are compared against a lookup table of possible dimuon roads. If a particular set of hits across the four stations passes this logic, then the set of hits is sent to the Level 2 trigger logic. The Level 2 trigger, which is a single v1495 board, outputs the final stop trigger sent to the Trigger Supervisor (TS) on the main DAQ. When the TS decide to take the trigger, the TS send a trigger accepted signal to all the TDCs as a stop trigger.

The Time between the hits on the hodoscopes and the stop signal is the trigger delay time. The trigger delay time is slightly different for each subdetector. The range is between 800~1000 ns, and the difference between each subdetector is due to the different cable length. The wire chamber data are sent to TDC via level shifters that convert the outputs from the Amplifier Shaper Discrimina-

tor (w/charge) (ASDQ) into a Low Voltage Differential Signaling
(LVDS) signal that the TDCs take. The proportional tube signals
are also sent to TDCs via a custom made amplifier cards.

There are three DAQ machines. The spill-counter script puts the
spill-counter in a text file and shares with all 3 DAQ system.

2.8.1   CODA

Both Scaler DAQ and the Main DAQ are driven by the CODA
(CEBAF On-line Data Acquisition) system developed at JLab[54].
In the Main DAQ, the CODA arranges all detector channels from 13
Readout controllers (ROCs) to Event Builder; for Scaler DAQ, there
is only one ROC. The event transfer (ET) is a stand-alone package
which sharing data buffers between programs. Event recorder then
stores the data into the harddisk in special CODA data format.
The raw data format is programed with the Experiment Control
System (Afecs) which come with a platform and its own language:
crl. With the Event IO (evio) library, the user can write their own
decoder to decode the CODA raw data to the data format they
want. SeaQuest is using c++ based decoder and the decoded data
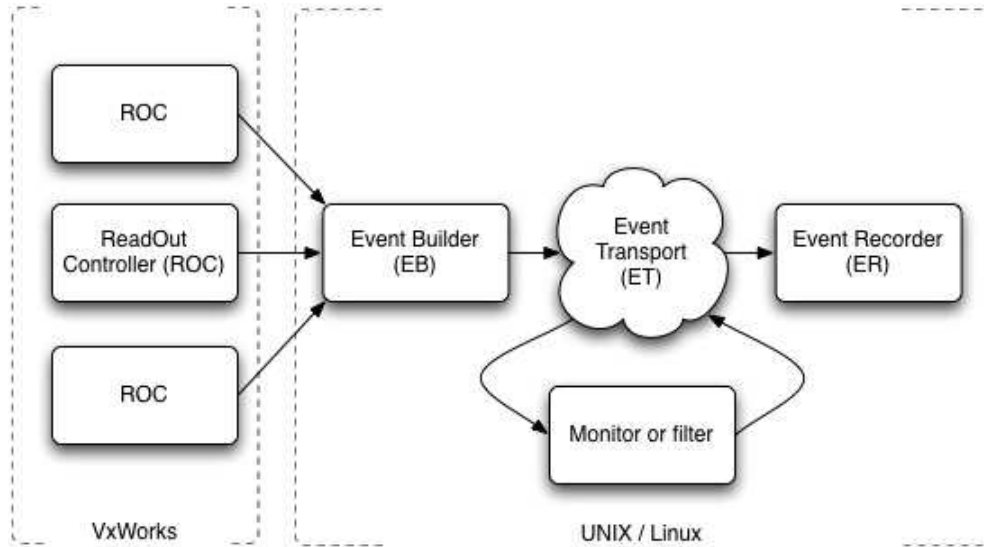
Figure 2.8: CODA diagram[54].

is stored in the MySQL database.

2.8.1.1 ROC

The ROC is basically a VME CPU. There are three kinds of CPU at SeaQuest. Linux-based CPU is one of them. Two of them are VX-Works based, MVME5500 and MVME6100. The difference between them is readout rate. MVME6100 is faster than MVME550 for a factor of two. However, Since CDF was using MVME5500, there are lots of spare modules. SeaQuest keeps some MVME5500 as spare modules. Scaler DAQ is also using MVME5500. Since Scaler

DAQ is deadtime free, so that a slower CPU is acceptable. The MVME5500 also used in the stand-alone test station for electronics test. The VXWorks CPU doesn't have it own system installed in the CPU board. Every time when it boots up, it will connect with the mother Linux box to read the boot file and to load drivers for front-end-electronics. All the drivers need to be compiled at the VXWorks machine at Jlabs and all crl code need to be compiled at the mother Linux PC before loading to the VXWorks.

Another one is Linux based. It is no longer using the crl language, but use c instead. All the driver and code are compiled in the single-board CPU. The Linix CPU has better radiation-hardened.

2.8.2   Scaler DAQ

The Scaler DAQ is a standalone DAQ that is designed to monitor the quality of the beam coming into SeaQuest. The trigger used is a 10kHz pulse from a gate-generator (LeCroy Model 465), and the signal monitored is one of the hodoscope planes. There are 4 VME scalers installed on the Scaler DAQ, one of which (Scaler1) is used for the purpose of monitoring the beam quality. The hodoscope hits

are counted in the VME scaler, and the buffer is read and cleared at each 10kHz trigger. This allows us to indirectly monitor the fluctuations in the beam intensity at 10kHz. Performing an FFT during Run1 showed significant 360Hz and subharmonic components in the beam, which created problems for our detectors by increasing the hit multiplicity. The Scaler DAQ is a single-VME system which does not have a TS or a TIR, but rather has a SIS3600 standalone trigger interface card. The other 3 VME scalers (Scalers2-4) on this DAQ are used to monitor per-spill rates such as trigger rates, RF counts, prescaled trigger rates, target positions, etc. These 3 scalers are enabled-to-count at the BOS, and are stopped and read at the EOS. The BOS and EOS are sent into two of the scaler channels in Scaler1. The EOS is also OR'd with the 10kHz trigger to create the trigger for the scaler DAQ. When reading out Scaler1 at 10kHz, the CRL file is coded to monitor the two scaler channels holding the BOS/EOS. If either of these channels sees a hit, then the command is issued by the CRL to either enable counting (BOS) or readout (EOS) for Scalers2-4. After being read, the scaler buffers are cleared, a re-enabled for counting. Therefore, Scalers2-4 only appears twice in the data stream per spill.
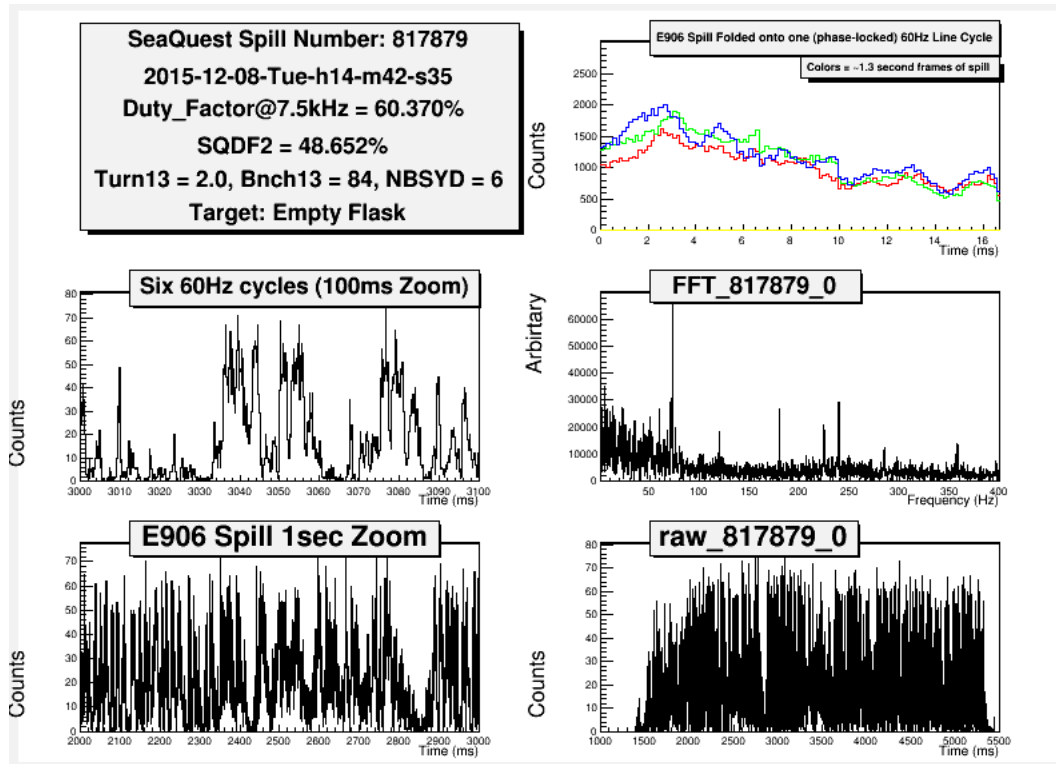
Figure 2.9: Scaler DAQ information for each spill

The read out of the VME-based DAQ is done using CODA. An independent program analyzes the data in realtime to monitor the performance of the detector and trigger, as well as the quality of the beam. [http://e906-gat6.fnal.gov:8081/SeaQuestAcc/] The example of the plot of the quality of the beam is shown in the figure2.9.

2.8.2.1   Deadtime free

The data from the Scaler DAQ is often used by the Accelerator Division to monitor and tune the beam. The FFT information calculated from the Scaler DAQ is viewable from outside via a website. This means that the data analysis must have a high enough turnaround time so that those tuning the beam have up-to-date information. To this end, a Scaler Realtime Monitor has been written in ROOT that grabs the Scaler DAQ data directly from the data stream before it is even written to disk. The portion of the code that grabs the data is called ETSpy. It latches to the Event Transfer (ET) function of CODA in order to grab the data directly. The CODA ET system is a function that allows multiple "stations" to receive data from the data stream. When a ROC sends data to CODA over Ethernet, it is first written to a buffer in the ET. This buffer is passed from one "station" to the next until there are no more stations, and the buffer is returned to "Grand Central Station" for use for another event. The number and size of the buffer can be set by the user. For the Scaler DAQ, the realtime monitor station is created after the CODA station. The CODA station

takes the data and writes to disk, while the realtime monitor station is designed to send the data directly to memory as defined by the ROOT script. The realtime monitor station is set to run in BLOCKING MODE, which means it will read every buffer. This means that if the realtime monitor falls behind in processing the events, the events coming from the ROC will have to remain in the ET buffer until it is read by this station. Note that if the number of events that needs to be retained is larger than the number of buffers available, then this will appear as deadtime in the front-end electronics (ROCs). In order to avoid this situation, the number of available ET buffers is set sufficiently large enough such that the entire 10kHz x 5 second spill can be retained in the ET buffer. Typically, the realtime monitor can keep up in realtime.

2.8.3   Beam DAQ

The Beam Cerenkov DAQ is designed to perform the same function as the Scaler DAQ in that it is used to monitor the beam quality. However, this DAQ receives a more direct measure of the beam quality by inserting a Cerenkov monitor directly into the beamline.

The trigger used for this system will also be the RF clock coming from the Accelerator, which means we will receive a bucket by bucket measure of the beam intensity. The beam Cerenkov DAQ is not using CODA, but rather a custom made readout board (QIE) designed to allow LVDS outputs to Scaler-Latch (SL) as well as Ethernet access to directly access the data from a Linux host. The Beam Cerenkov DAQ will perform a multitude of functions. It receives 53MHz RF clock as a trigger, and monitor beam intensity in each RF bucket. It also receives the EOS (or BOS), and count it in a non-volatile memory. This will be the common spill count (spillID) across all of our DAQs. It retains all 53MHz x 5sec data in its memory for fast readout. All this while keeping track of a running sum of I and I^2. At EOS, BeamDAQ calculates duty factor N%, and output N NIM pulses to ACNET.

The realtime monitor for this DAQ will be written in ROOT. However, since the data volume for each 5 second spill is expected to be large (˜300 MB without zero suppression), we will not keep all of this data. At EOS, the script will open a TCP socket to the Cerenkov board's Ethernet interface, and begin retrieving data. With the data, the script will create histograms of 5000 bins over

5 seconds (1kHz), 50000 bins over 5 seconds (10kHz), 50000 bins over 0.5 seconds (100kHz), 100000 bins over 0.1 seconds (1MHz) and a FFT of each of the above 4 histograms. It also creates a histogram of (588 x N main injector turns) bins, where 588 refers to the number of RF buckets in one main injector turn. The 588 bin histogram is designed to see the uniformity of the beam occupancy per bucket across the main injector turn. In total, the 5 raw histograms of differing frequencies and their FFTs, both of which are type TH1F, is expected to take up about 1.7MB of memory and disk space to save. The BeamDAQ also retrieves the dutyfactor from the Cerenkov readout board, and output to EPICS. All the histograms and the dutyfactor are saved to the rootfile. For each physics event, BeamDAQ retrieve each trigger event recorded +/- 16 RF buckets, and save as vectors into a ROOT Tree and an ASCII file. The block of QIE data for all buckets is about 300 MB. To read this much data in time to analyze it and be ready for the next spill, the DAQ program uses boost's implementation of multithreading. The analyzed data is displayed on a public webpage so that shifters and accelerator operators can monitor the quality of the beam. An example of the webpage is shown in the figure2.10.
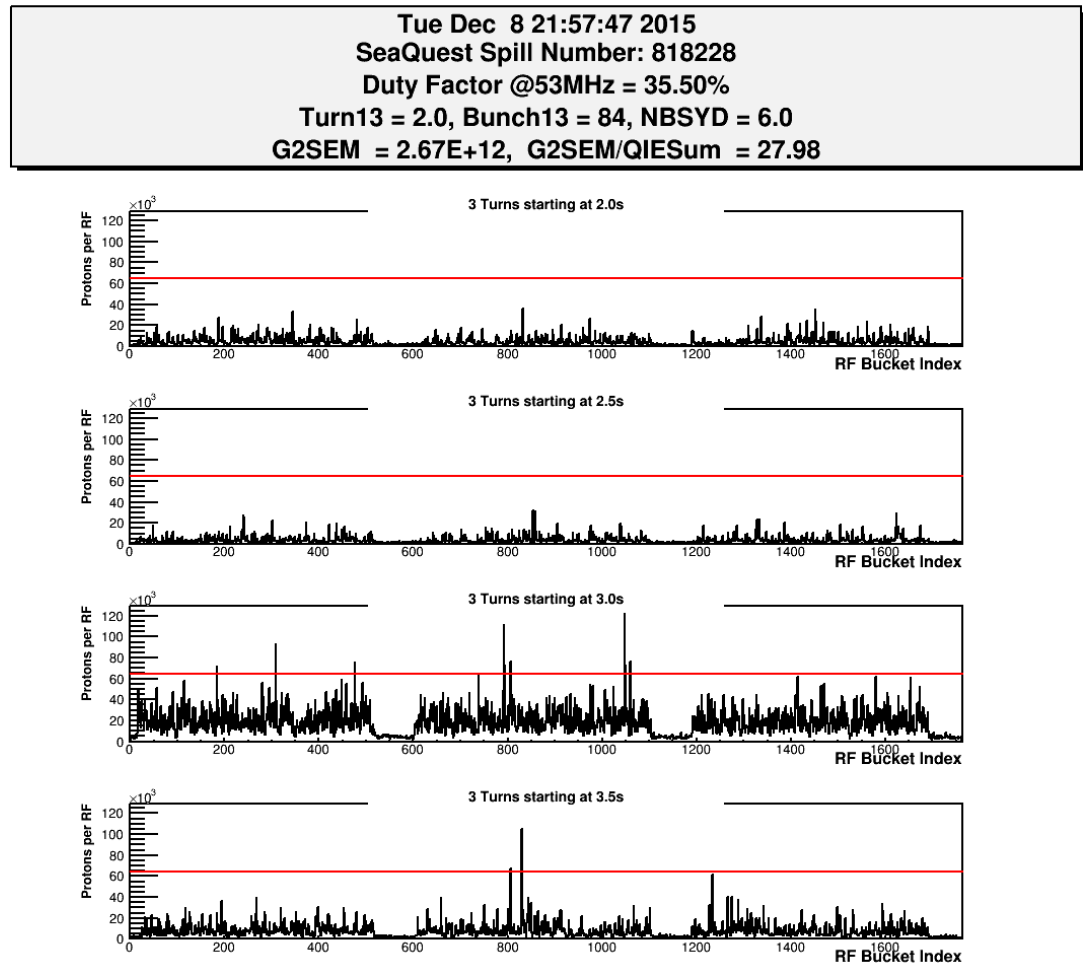
Figure 2.10: An example of the Beam DAQ webpage.

In addition to the stand-alone DAQ program, the QIE board outputs the intensity of the ± 16 buckets surrounding each trigger into the Main DAQ through a latch TDC.

2.8.3.1   Deadtime free

All of above must be performed within the 55 seconds before the next spill appears. It is important to note that the beam Cerenkov readout board also acts as the spillcounter for the experiment. Each beam spill will be assigned a unique ID which will be written to all 3 DAQ systems to synchronize the data-taking process.

2.8.4   Main DAQ

The TS could receive up to 12 different kinds of triggers. First 4 triggers (MATRIX1-4) can be prescaled up to 24 bits. The second 4 triggers (MATRIX5, NIM1-3) can be prescaled up to 16 bits. The rest of the triggers (NIM4, flush trigger, BOS,EOS) are not prescalable. The main DAQ decides which trigger the TS could receive and prescale factor. Addition to that, for the FPGA triggers and NIM1 trigger, there is also a inhibit signal from the QIE board; when the beam intensity is higher than the threshold, as the redline in fig2.10, QIE will send a inhibit signal to MainDAQ and this event won't trigger the trigger the TS. Once the TS receives the trigger,

it will count the prescale factor and decide if the main DAQ is able to accept the trigger or not. Once the TS accepts the trigger, it gives an "accepted trigger" signal as the reference to the other front end electronics, such as stop signal for TDC. The TS also connects to the Main DAQ system through the internet. The TS connects with TIR on each VME crate. Each VME crate also connects to the Main DAQ through the CPU internet port. We also name each CPU as ROC (readout controller). When the TS accept a trigger, it will acknowledge the TIRs, and each TIR sends an interrupt to corresponding ROC. The ROCs will then start reading the FEEs.

The TS also sends trigger to QIE, and the QIE retains ± 16 RF buckets around that trigger to see the beam quality around each of our event triggers. Output this array in an encoded format to a scaler-latch. If the beam intensity in RF buckets neighboring the trigger is higher than the user-select threshold, then the board will issue a veto signal to the TS to ignore this trigger.

2.8.4.1   Deadtime

Since the Main DAQ is using the interrupt, the interrupt causes
about the 10 μs deadtime.   The TDC has a 32 μs of copy-in-
progress (CIP) time. So even if we readout nothing, the slowest
FEE is TDC, which is the main source of deadtime. When the TS
decides to accept the trigger, it will wait for 30 μs before it sends an
interrupt to TIRs. So that even we readout nothing, the deadtime
is about $42\mu s$. The TDC readout time is the main source of dead-
time in Main DAQ. The average TDC readout time is about 300 ns
per 32bits (one hit). The slowest ROC contents 7 TDCs which in
average has 150 μs deadtime including the 42 μs initial deadtime.

2.9   Decoder and MySQL Database

After the the DAQ save the raw data in the CODA data format,
the C++ based decoder will collect the raw data from three DAQ
machines and also collect the slowcontrol information, and decode
the data then save to MySQL database. The raw data will be kept

forever, and if one found that decoder could be improved, SeaQuest will make another production of decorded data and upload it to the MySQL database. The version for this analysis is R005 V001. It is simply the most up to date production we have now.

2.10 Event reconstroction

The event reconstruction used the track fitting and vertex fitting based on the Kalman filter, which is referring as kTracker. An example of dimuon reconstruction is shown as Figure 2.11.
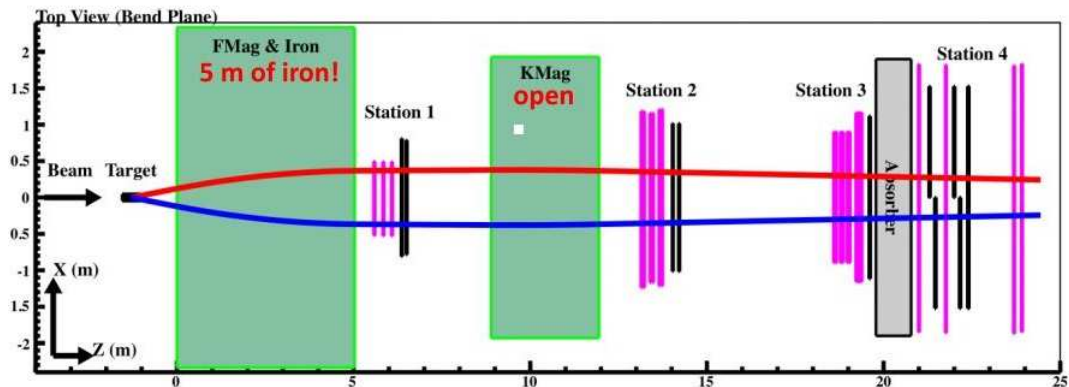
Figure 2.11: dimuon reconstroction example

First step to remove the out of time hits, after hits, and clustered hits. The second step is to apply the basic event quality cut, which is to remove the high multiplicity events. In the Chamber, U

and U' belongs to one view; X and X' belongs to one view; V and V' belongs to one view. Next step of kTracker is to build a triplet between station 2 and 3. It will request at least one hit per view and at least 4 hits per station. Then the station 2 and station 3 hodoscope masking will be applied, which means that kTracker checks the neighbouring hodoscopes are also fired. Then the kTracker will extend to the station 4 proportional tubes to find if this track fired the muon identification or not. It all checks hodoscope masking for station4 hodoscopes. After the hit information from station 2,3,4 are collected, it project back to station1. The kTracker then start to use Kalman filter method to iteratively remove the hits with bad fitting quality. Then the track swims through the magnet, back to the vertex point and does vertex fitting with dimuon tracks. The flow chart is shown as Figure2.12 [55].
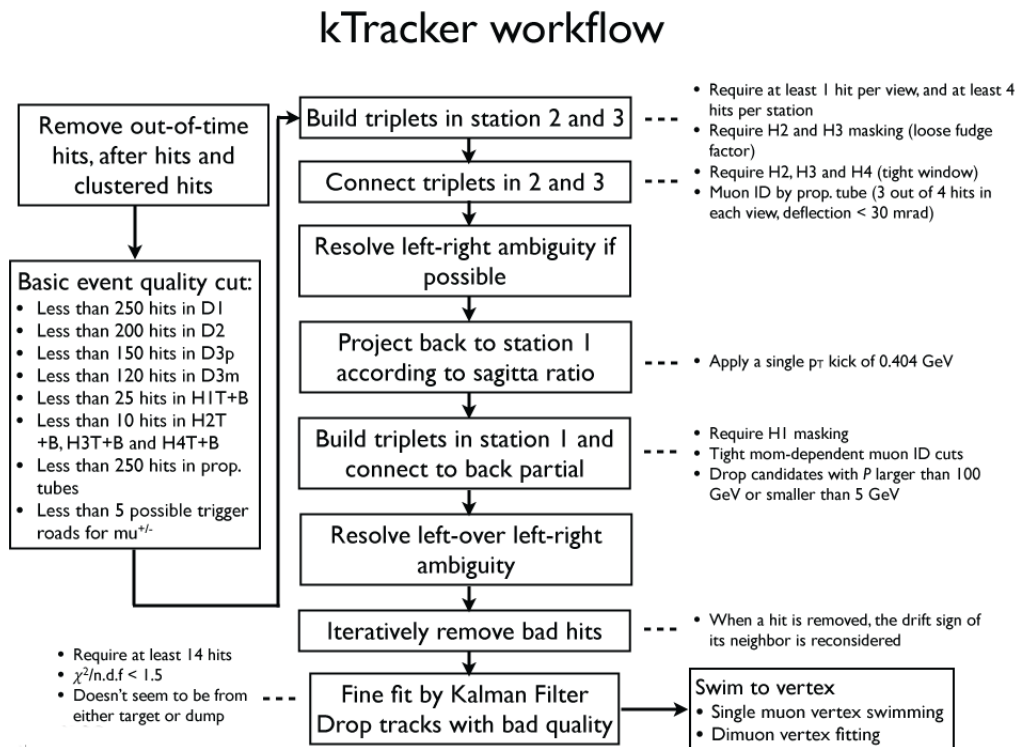
Figure 2.12: kTracker workflow

2.11 Experiment timeline

After the commissioning at Run1 at 2012. SeaQuest has upgraded the trigger, DAQ system, TDC and the beam monitor. The first physics run (Run2) of SeaQuest experiment started at 2013. The accelerator group keeps working on improving the uniformity and duty factor of the proton beam. At the end of 2014, the accelerator group found that the major problem is the QXR setup, thus the beam quality was improved significantly. The new Station 1 chamber was installed at the beginning of Run4 at the end of 2015. The data in this study is highlight by the blue box in Fig. 2.13.
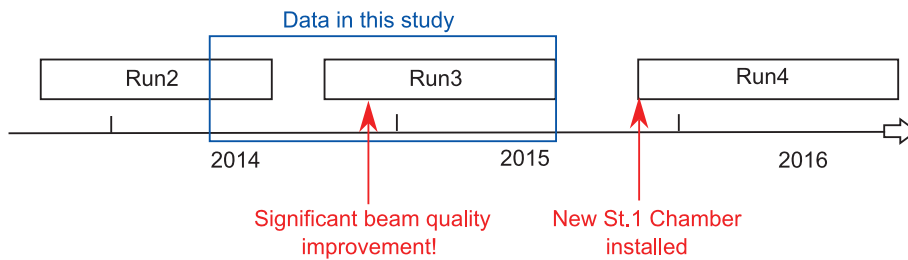
Figure 2.13: SeaQuest timeline.

Chapter 3

Analysis

This study is using prodution R005 V001, which is the lastest version of production until Run3 data. For the p_T suppression study, the solid targets were chosen. For the D/H study, Since the purity of LD2 is improved from Run3, only the the data sets 67 was used.

This analysis flow is to apply the official SeaQuest cut to remove the bad spills and to find good dimuon tracks from the target region. After the dimuons are selected, a mass spectrum fitting based on Monte-Carlo and background study will be applied to find yield (number of events) of each process. The relative cross-section of each target could be found with the yield of each process of each target. The ratio between the different targets for each process, such as Drell-Yan,J/Ψ or Ψ', could be calculated by the relative

cross-section for each target and the α value of each process could be found with the ratio. The systematic error will be estimated with according to background estimation and rate dependence effect.

3.1   Data Sets

For the p_T suppression study, the solid targets were chosen. The live-protons is the number of protons after spill selection in SeaQuest official cut. The live protons is an important number for cross check and it will be used for normaling the cross-section of each target.

Data Set	L1	L2	live protons (C)	live protons (Fe)	live protons (W)
Run2	57+59	13	1.62e+16	5.27e+15	5.41e+15
Run3a	62	13	1.24e+16	6.47e+15	6.52e+15
Run3b	67	13	3.67e+16	1.79e+16	1.83e+16

Table 3.1: The number of live proton for each solid target of each data set

3.2   SeaQuest Official Cut list

The Data Cut is following SeaQuest official cut list for R005[57][58]. The cuts are applied after event reconstruction. The official SeaQuest

cut list is to remove the bad spills and to find good dimuon tracks from the target region. It is also to make sure all analysis was done in the same standard so that it will be easier to compare different study result. Reasons of cuts are the followings:

3.2.1 Spill Selection

The official SeaQuest Cut list can be found in the Ref.[59]. This is a list which remove the number of spills which doesn't contain full information , such as target position, beam intensity, or the non-physics runs, such as trigger testing run or DAQ testing runs.

3.2.2 Event Selection

The Physics events has to fire physics trigger (FPGA1). This is referred as the trigger masking during the event reconstroction.

3.2.3   Track Selection

Becuase there are 18 detector planes, if a tracker fired all detector, the number of hits for that track is 18. Considering the efficiency of detector and tracker, the number of hits in each track is required to be larger then 14[60]. The starting Z (beam direction) position of a track is constrained according to the Monte-Carlo simulation. After reconstrucation, the tracker will check the hodoscope masking again, and the track has to pass the trigger matrix (FPGA1 trigger).

3.2.4   Dimuon selection

Dimuon vertex position, both the x and y are constrained to 0. ± 2 cm, and z is constrained to be between -300 cm and 200 cm according to the target and dump position. According to the GMC result, the dimuon 3-momentum at vertex position after re-tracking is constrained. The knimatic values also need to be within reason by its defination, for instance we have $0. < x_{beam} < 1.(x_{beam} = x1)$, $0. < x_{target} < 1.(x_{target} = x2), -1. < x_F < 1$. Also to make sure that two trackers come from the same vertex and the difference

of the single-muon z position should be less than 250 cm. Also the chisquare of the dmuon fitting is constrained according to the Monte-Carlo simulation (less than 15.).

3.2.5 Target/Dump selection

The dump data is not used in this analysis, however, for the target dimuon, the z position of vertex point is constrained at target region, $-300cm < dz < -60cm.$, according the GMC. During the vertex fitting, the chisquare of vertex fitting of a target dimuon should be smaller than the chisquare of vertex fitting of a dump dimuon.

3.3 Dimuon Counting

Once we have the mass spectrum of reconstructed dimuons, we can use the Kernel Estimation method[61] with RooFit package. Kernel estimation provides an unbinned and non-parametric estimate of the probability density function from which a set of data is drawn. The

number of DY, J/Ψ, and Ψ' events can be estimated by fitting the histogram with a combination of Gaussian distributions for J/Ψ and Ψ' peak, Monte Carlo histogram for Drell-Yan process , and random background. The goal of non-parametric methods is to remove the bin-width-dependence of the estimator.

3.3.1   DY Histogram from Monte Carlo

We refer to our Monte Carlo framework as GMC, for Geant4 Monte Carlo simulation. It uses the Geant4 toolkit to simulate the response of our spectrometer to both dimuons and background particles. A standard physics list provided by Geant4 is used to simulate physics after dimuon generation.

3.3.1.1   Dimuon Generation

We generate the dimuons with a flat distribution in mass and x_F,then give them a weight based on their leading order cross section. Considering the computing power and the amount of simulated statistics

we need, a next-to-leading-order (NLO) cross section calculation for the weighting is not taken into account. In order to calculate this weight correctly a PDF set is needed. GMC uses the LHAPDF software package to look up the PDFs and we use the CT10nlo set. The dimuons are generated with a flat distribution in x_F and mass, and the variables x_{beam} and x_{target} are calculated from these variables. p_T and Collins-Soper theta and phi are thrown according to their distributions and do not affect the weighting. A z position along the beam line is chosen according to a distribution based on beam attenuation. Mass, x_F, p_T, z, and the Collins-Soper angles are sufficient to determine the kinematics of each muon. GMC is capable of generating dimuons according to Drell-Yan distributions.

3.3.2 Gaussians for J/Ψ and Ψ'

The J/Ψ ans Ψ' distribution is discribed by the Gaussians distribution in the fitting. The mass of J/Ψ is 3.096 GeV, and the mass of Ψ' is 3.686 GeV. Since the Monte Carlo simulation doesn't have the same backgound with the real data, the reconstruction efficiency and the detector efficiency is different with the real data; therefore

the Monte Carlo simulation cannot describe the mass resolution very well. The mass distribution of DY process is broad so that using the Monte Carlo in the mass spectrum fitting is not sensitive to resolution. For J/Ψ and Ψ' mass spectrum is narrower, we use a Gaussian. The mean mass and sigma of Gaussian of J/Ψ are adjustable, and mass and sigma of Gaussian of Ψ' is a fixed ratio (3.686/3.096) to J/Ψ.

3.3.3   Combinatorial Background

One of the background sources is the combinatorial background from pion and kion decays before they interacts with hadron absorber. To evaluate it we use the same-sign muon pairs. When the ktracker found only one muon track in a regular physics event (FPGA1), this single muon is saved to a special root file and random-mixed with another different-sign muon in the same physics run, which is mix-event. By collecting the mix-event over one data set, we can get the combinatorial background shape. We also collected the same-sign dimuon while data taken with the different trigger (FPGA3, prescale=123). With the number of same sign trigger, we

can estimate the number of events of combinatorial background. In the mass spectrum fitting, the shape of the histogram came from mix event, the number of combinatorial backgrounds events is fixed by the number of the same-sign triggers with the following relation[ref]:

$$N_{\mu^+\mu^-}^{Bg} = \frac{2 \bullet 123}{N_{mix}} \sqrt{N_{\mu^+\mu^+} N_{\mu^-\mu^-}} \tag{3.1}$$

3.3.4 Mass Spectrum Fitting

The mass spectrum from the real data of the different p_T region and the different target can be fitted with four parts, namely DY, J/Ψ, Ψ', and background. Fig. 3.1 shows the example of mass spectrum fitting. The black line is the combinatorial background. The red line is the J/Ψ Gaussian. The green line is the Ψ' Gaussian. The pink line is DY from GMC. The mass spectrum fitting of each run of each target and p_T-bin are shown as Fig3.2, Fig3.3. and Fig3.4. The raw yield of each them are shown in Table 3.2,3.3, and 3.4.
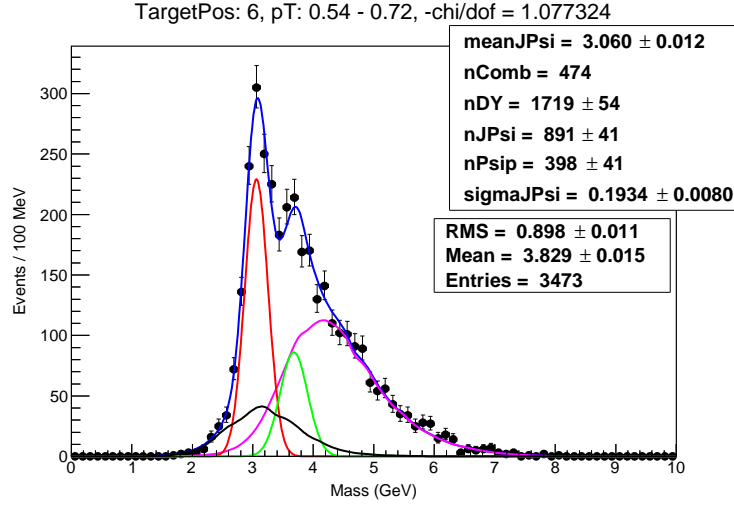
Figure 3.1: Example of mass spectrum fitting. The Black point is the data point. The data are from carbon target at $0.54 < pT < 0.72$. The black line is the combinatorial background. The red line is the J/Ψ Gaussians. The green line is the Ψ' Gaussians. The pink line is DY from GMC.

p_T Bin	1	2	3	4	5
Data-Set 67/C	1698±56	1703±56	1719±54	1801±55	1726±56
Data-Set 67/Fe	1855±61	1961±61	1848±58	2077±60	2079±62
Data-Set 67/W	2212±65	2406±66	2118±62	2603±66	2760±69
Data-Set 62/C	477±30	561±31	496±29	593±31	640±32
Data-Set 62/Fe	521±32	610±34	627±33	720±34	751±35
Data-Set 62/W	665±36	700±38	734±37	807±38	829±37
Data-Set Run2/C	568±33	517±32	529±32	568±31	518±33
Data-Set Run2/Fe	404±29	428±34	411±28	546±29	433±28
Data-Set Run2/W	498±31	480±31	534±31	551±31	681±33

Table 3.2: Table of all mass spectrum fitting result ($N_i(pT)$ of Drell-Yan)

p_T Bin	1	2	3	4	5
Data-Set 67/C	1414±50	1229±45	891±41	828±46	419±39
Data-Set 67/Fe	1289±47	1081±45	827±42	829±43	384±40
Data-Set 67/W	1198±47	1066±46	899±43	463±54	449±41
Data-Set 62/C	355±24	337±22	261±23	213±23	157±20
Data-Set 62/Fe	312±26	345±24	291±23	279±24	151±21
Data-Set 62/W	279±23	252±25	233±23	204±23	75±15
Data-Set Run2/C	426±28	471±30	361±26	364±25	167±48
Data-Set Run2/Fe	280±23	280±40	270±21	180±26	90±24
Data-Set Run2/W	247±26	281±25	201±24	249±23	150±23

Table 3.3: Table of all mass spectrum fitting result ($N_i(pT)$ of J/Ψ)

p_T Bin	1	2	3	4	5
Data-Set 67/C	484±47	437±47	398±41	406±48	397±46
Data-Set 67/Fe	439±50	426±50	399±49	319±50	591±49
Data-Set 67/W	433±54	424±54	443±51	463±54	622±51
Data-Set 62/C	171±26	151±23	143±25	162±26	109±24
Data-Set 62/Fe	136±30	150±27	101±26	182±28	213±26
Data-Set 62/W	137±29	125±32	96±30	107±30	124±25
Data-Set Run2/C	195±27	248±29	181±27	198±25	175±48
Data-Set Run2/Fe	133±25	162±26	101±22	153±30	180±25
Data-Set Run2/W	187±29	197±28	173±27	166±27	180±25

Table 3.4: Table of all mass spectrum fitting result ($N_i(pT)$ of Ψ')

3.4   Cross Section

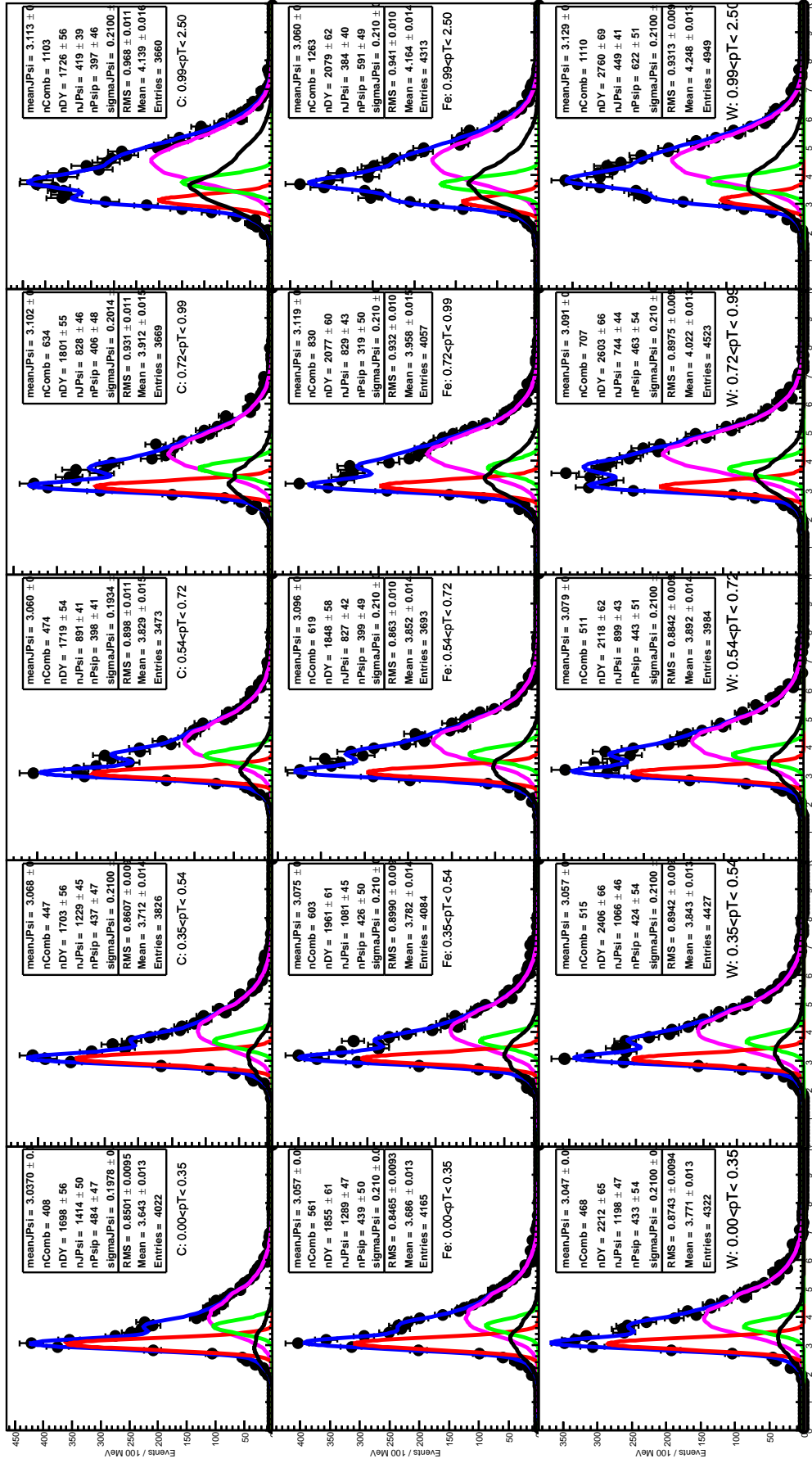The cross-section for this analysis for each target i at various kinematic bin is defined by

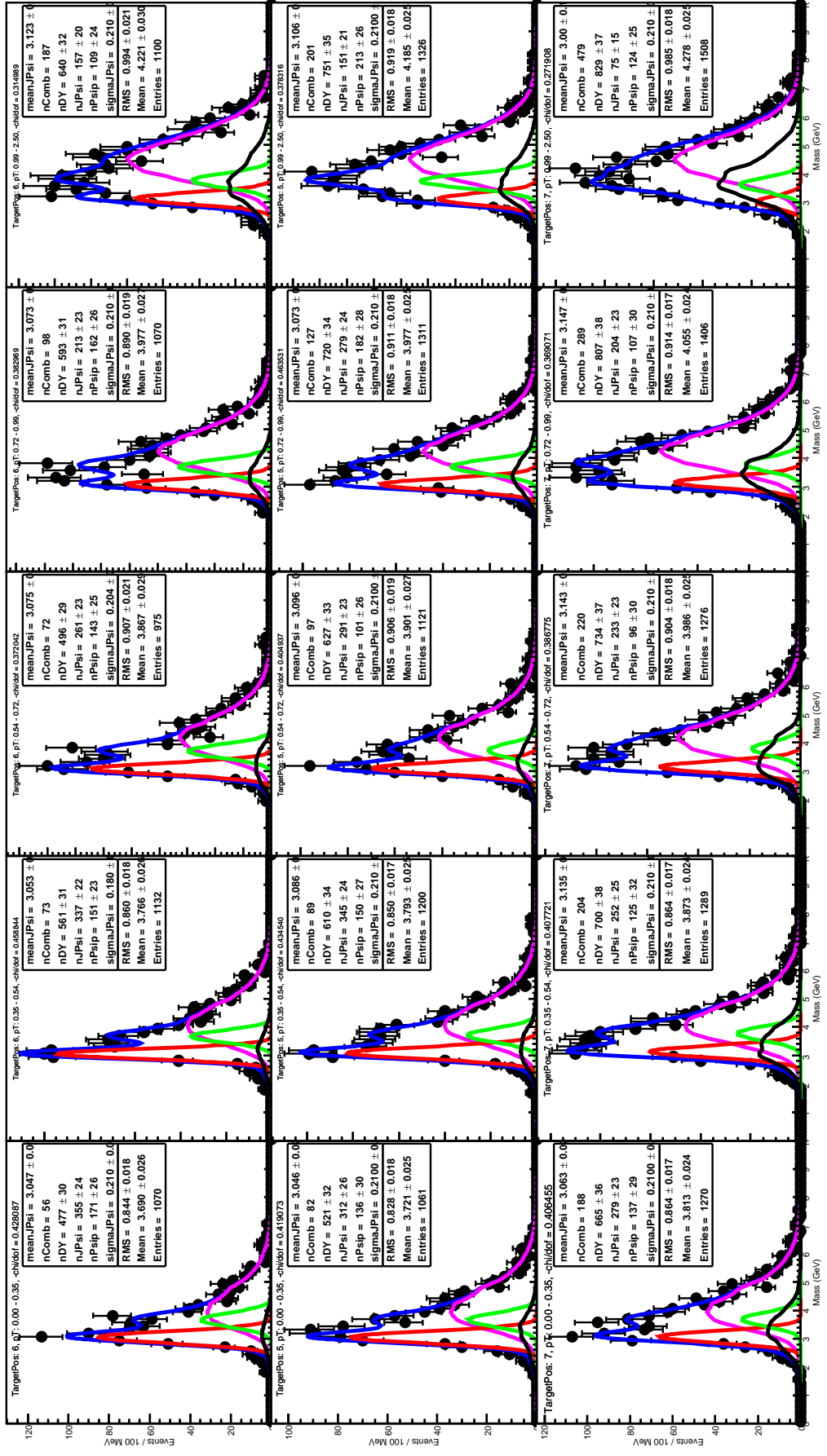Figure 3.2: All mass spectrum fitting of Data-set 67.

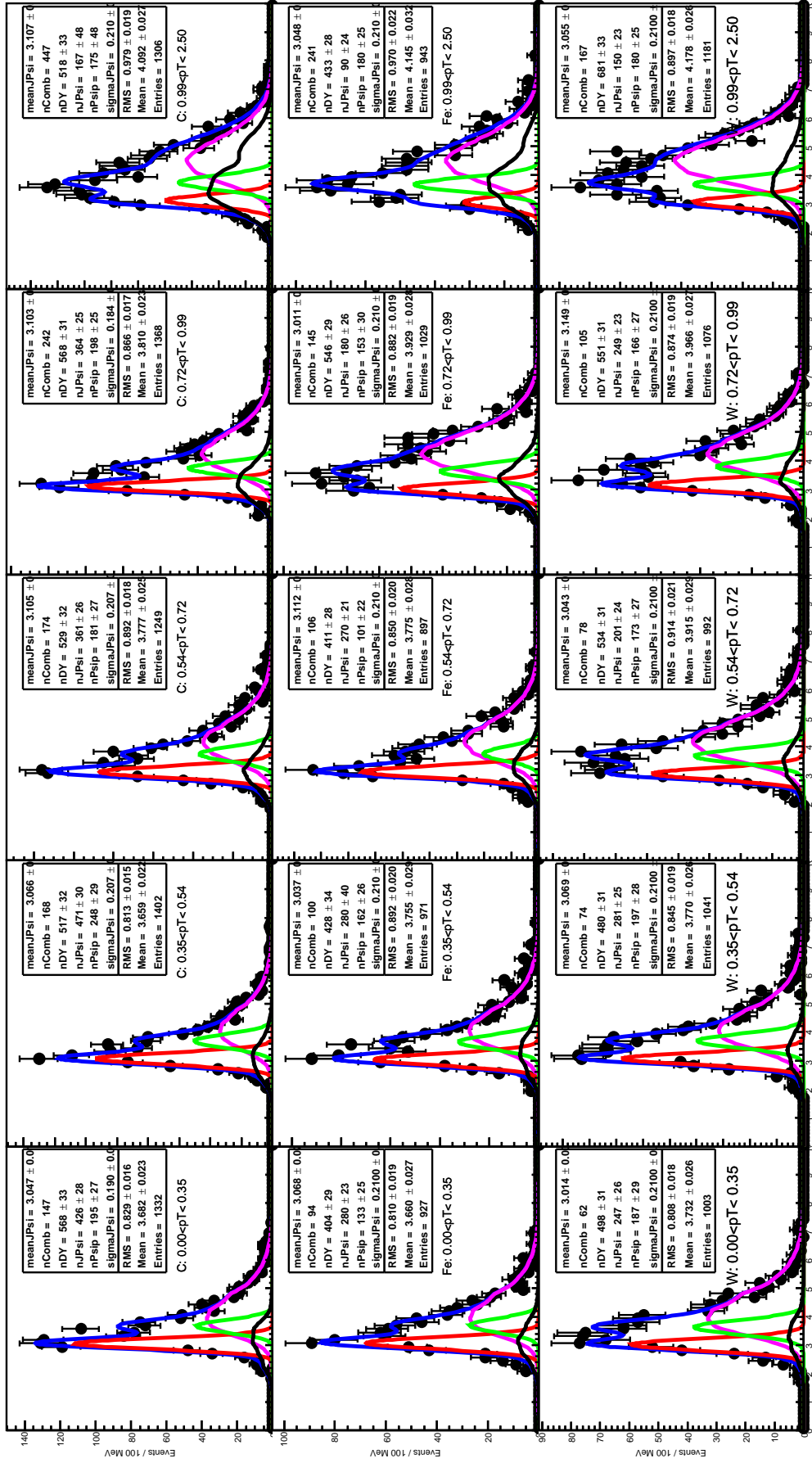Figure 3.3: All mass spectrum fitting of Data-set 62.

Figure 3.4: All mass spectrum fitting of Data-set Run.

$$\sigma_i(p_T) = \frac{N_i(p_T)}{L_i}, \tag{3.2}$$

$$L_i = I_i \cdot \rho_i \cdot \lambda_i \cdot \mathfrak{R}_i / A_i, \tag{3.3}$$

and

$$\mathfrak{R}_i = 1 - exp(-T_i/\lambda_i) \tag{3.4}$$

Where λ_i is nuclear interaction length, N_{ij} is the number of dimuon of each process for the target, i, and kinematic bin, j, L_i is the luminosity, ρ_i is the target density, T_i is the target thickness, I_i is the live protons, which listed at table 3.1 ,and it is the total number of incident protons for that target, and $\mathfrak{R}_i$ is the beam attenuation in the target. It is important to use the cross-section normalized to per nucleon so the cross-section becomes

$$\sigma_{Ni}(p_T) = \frac{N_i(p_T)}{L_i \cdot A} = \frac{N_i(p_T)}{I_i \cdot \rho_i \cdot \lambda_i \cdot \mathfrak{R}_i} \tag{3.5}$$

The value that we are using is listing in the Table3.5.

	H	D	C	Fe	W
T (inch)	20.	20.	0.436×3.	0.25×3.	0.125×3.
$\rho(g \cdot cm^{-3})$	0.07065	0.1617	1.802	7.874	19.3
$\lambda \cdot \rho \; (g \cdot cm^{-2})$	52.0	71.8	85.8	132.1	191.9

Table 3.5: Parameters for cross section calculation. There are 3 pieces of each solid target, so that the thickness of them are listed differently.

3.5   Ratio for Each Data Set

Since we only need the cross section to get the ratio between different targets, the absolute-cross-section is not necessary. The ratios are calculated for iron and tungsten by dividing their cross-section against the carbon target. Note that the cross section is normalized to per nucleon so that the ratio is also the ratio per nucleon, which could be written as :

$$R_{FeN} = \frac{\sigma_{Fe}/A_{Fe}}{\sigma_C/A_C} = \frac{\sigma_{Fe}/A_{Fe}}{\sigma_C/12.0107}; \tag{3.6}$$

$$R_{WN} = \frac{\sigma_W/A_W}{\sigma_C/A_C} = \frac{\sigma_W/A_W}{\sigma_C/12.0107}; \tag{3.7}$$

3.6 Systematic Error

There are two main sources of systematic error, background estimation and the rate dependence.

3.6.1 Background estimation

The number of the combinatorial background events in the mass spectrum fitting is $N^{Bg}_{\mu^+\mu^-}$ in Eq. 3.8. The error of this number was not considered in the mass spectrum fitting. The statistic error of background ($dN^{Bg}_{\mu^+\mu^-}$) is from the number of FPGA3 events, as shown as following equation.

$$dN^{Bg}_{\mu^+\mu^-} = \frac{N^{Bg}_{\mu^+\mu^-}\sqrt{N_{\mu^+\mu^+}+N_{\mu^-\mu^-}}}{2\sqrt{N_{\mu^+\mu^+}N_{\mu^-\mu^-}}} \tag{3.8}$$

Two extra mass spectrum fittings were done following the equations.

$$N^{Bg+}_{\mu^+\mu^-} = N^{Bg}_{\mu^+\mu^-} + dN^{Bg}_{\mu^+\mu^-} \tag{3.9}$$

$$N_{\mu^+\mu^-}^{Bg-} = N_{\mu^+\mu^-}^{Bg} - dN_{\mu^+\mu^-}^{Bg}. \qquad (3.10)$$

With the different yeild of background ($N_{\mu^+\mu^-}^{Bg-}$ and $N_{\mu^+\mu^-}^{Bg+}$), the different yield of each process could be obtained. With different yield of each process, new corss section of each process could be obtained, such as $\sigma_{DY}^{Bg+}, \sigma_{J/\psi}^{Bg+}, \sigma_{\psi'}^{Bg+}, \sigma_{DY}^{Bg-}, \sigma_{J/\psi}^{Bg-}, \sigma_{\psi'}^{Bg-}$. The systematic error ($d\sigma_{DY}^{Bg}$) of cross-section is determined with the following formula and propagated with the calculation after we get cross-section:

if($\sigma_{DY}^{Bg+} - \sigma_{DY}^{Bg}$) > ($\sigma_{DY}^{Bg-} - \sigma_{DY}^{Bg}$) then

$$d\sigma_{DY}^{Bg} = (\sigma_{DY}^{Bg+} - \sigma_{DY}^{Bg}) \qquad (3.11)$$

if($\sigma_{DY}^{Bg+} - \sigma_{DY}^{Bg}$) < ($\sigma_{DY}^{Bg-} - \sigma_{DY}^{Bg}$) then

$$d\sigma_{DY}^{Bg} = (\sigma_{DY}^{Bg-} - \sigma_{DY}^{Bg}) \qquad (3.12)$$

3.6.2   Rate dependence

There is only one pair of clean dimuon in each Monte Carlo event. However, in reality, there are background hits. Those backgrounds

come from the following source. Each station of the drift chamber has its own drift time, the longest one is around 300 ns, which is about 16 RF buckets. The higher luminosity of each RF bucket usually results in more background hits and leads to lower reconstruction efficiency. The left plot in figure3.5 shows the clean Monte Carlo event, the middle one shows the event that we can still easily reconstruct. The left plot in the figure3.5 shows the event that we have a hard time reconstructing. On the other hand, our detector, electronic, DAQ, and trigger system has their own deadtime in prcessing hits too. All of them adding up, which lowers the possibility of getting the dimuon when luminosity is higher. This is what we called rate dependence.

3.6.3 Final systematic error

Since the background might have some rate dependence effect in it, those two kinds of systematic error might not be independent. There are a few rate depandence studies at SeaQuest group[63, 64, 66, 65]. The final systematic error simply adds the background error of each bin with 8% rate dependence[63]. The final systematic error
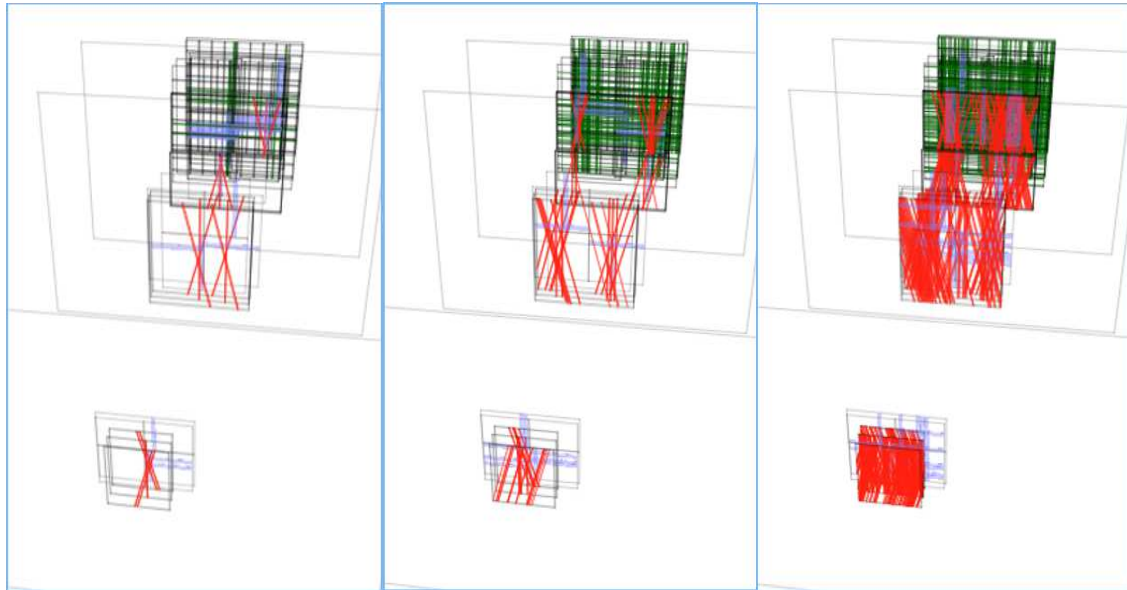
Figure 3.5: The plot at left hand side is From GMC. The plot in the middle is the ideal event, which is a real event for data. The plot on the right hand side is the dirty event from real data.

is then added to the ratio.

3.7   Merge different runs

Because the systematic error is different for each data-set, and it could cancel out while calculating the ratio, the data-sets are merged after we get ratio and applied systematic error. After we get the ratios for iron and tungsten of each data-set, the ratio of each data-set is then combined with the following formula:

target\p_T bin	1	2	3	4	5
DY					
Fe/C	0.033775	0.034376	0.032921	0.032278	0.033664
W/C	0.030876	0.031047	0.029411	0.029445	0.032063
J/Ψ					
Fe/C	0.031694	0.034233	0.042764	0.049819	0.081149
W/C	0.024335	0.025892	0.034277	0.037564	0.055589
Ψ'					
Fe/C	0.084542	0.088678	0.091509	0.097187	0.148142
W/C	0.070883	0.075236	0.082708	0.080693	0.112242

Table 3.7: dR_{merge} is the statistic error of R_{merge} in Eq. 3.13

$$R_{merge} = \frac{R_{run2}/dR_{run2}^2 + R_{run3a}/dR_{run3a}^2 + R_{run3b}/dR_{run3b}^2}{1/dR_{run2}^2 + 1/dR_{run3a}^2 + 1/dR_{run3b}^2} \quad (3.13)$$

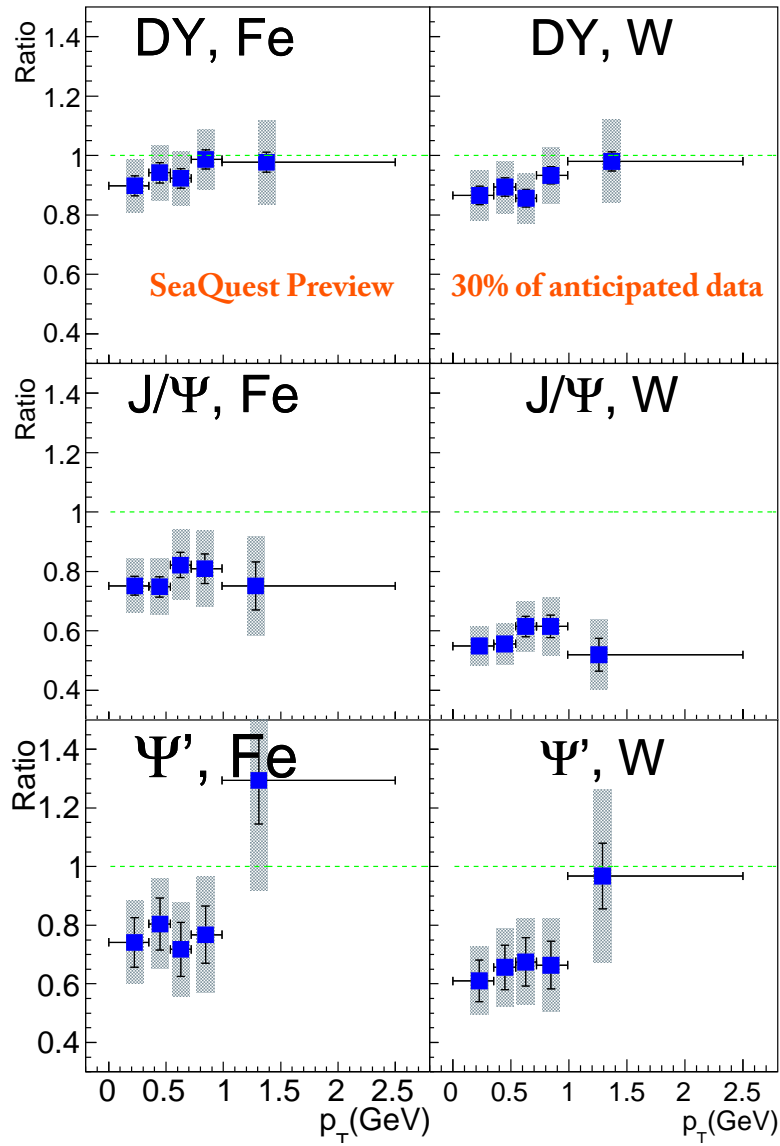| target\p_T bin	1	2	3	4	5
DY					
Fe/C	0.897623	0.941998	0.922984	0.986637	0.977397
W/C	0.865636	0.893964	0.856222	0.933266	0.980243
J/Ψ					
Fe/C	0.751443	0.748331	0.821606	0.809736	0.751433
W/C	0.548533	0.556304	0.614929	0.614968	0.519370
Ψ'					
Fe/C	0.741712	0.804564	0.717291	0.767551	1.293805
W/C	0.609735	0.655830	0.674586	0.663980	0.967870

Table 3.6: R_{merge} in Eq.3.13

Figure 3.6: Ratio after merge different runs

3.8 α

The α value is simply from the equation

$$\sigma_A = A^{\alpha_{pT}} \sigma_n \qquad (3.14)$$

A is the atomic mass of the target. σ_n and σ_A are the cross-section of the target and nucleon.

In our case, since the σ_n and σ_A is normalized to cross-section per nucleon, the q becomes

$$\frac{\sigma_A}{A} = A^{\alpha_{pT}-1} \sigma_n = A^{\alpha_{pT}-1} \cdot \frac{\sigma_C}{12} \qquad (3.15)$$

$$\frac{\sigma_A}{\sigma_C} \frac{12}{A} = A^{\alpha_{pT}-1} \qquad (3.16)$$

$$\ln(\frac{\sigma_A}{\sigma_C} \frac{12}{A}) = (\alpha_{pT} - 1) \cdot \ln(A) \qquad (3.17)$$

$$\ln(\frac{\sigma_A}{\sigma_C} \frac{12}{A}) + \ln(A) = \alpha_{pT} \cdot \ln(A) \qquad (3.18)$$

The Fig. 3.7 shows how the α value was obtaind. The y-axis of figure a is the left part of Eq. 3.18 and the x-axis is the right part of Eq. 3.18. The cross section ratio of Fe/C and W/C of each p_T bin was used to fit the α value. The fitting was done with only statistic

error to find out the statistic error for the α value, then done with both statistic error and systematic error to find the overall error. The fitting of each α value is shown in figures.
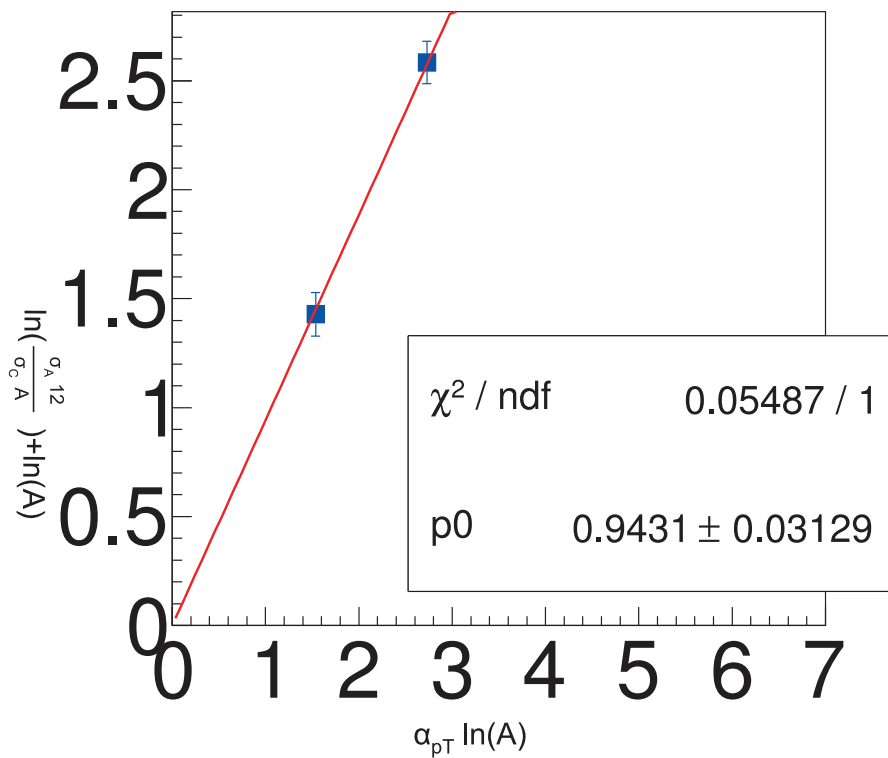

Figure 3.7: An example of α fitting. The y-axis of figure a is the left part of Eq3.18 and the x-axis is the right part of Eq.3.18. This plot looks like there are only two points. However, this function has to fit to Eq. 3.18, which means thus function must pass the point (0,0), so that is actually more like a 3 points fitting.
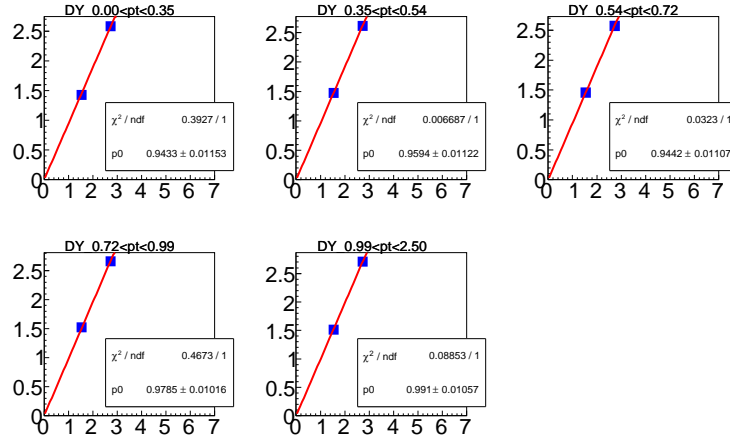
Figure 3.8: The α fitting for each p_T bin for DY process. The y-axis of figure a is the left part of Eq3.18 and the x-axis is the right part of Eq.3.18. This plot shows the fitting without systematic error

Figure 3.9: The α fitting for each p_T bin for DY process. The y-axis of figure a is the left part of Eq. 3.18 and the x-axis is the right part of Eq. 3.18. This plot shows the fitting with systematic error
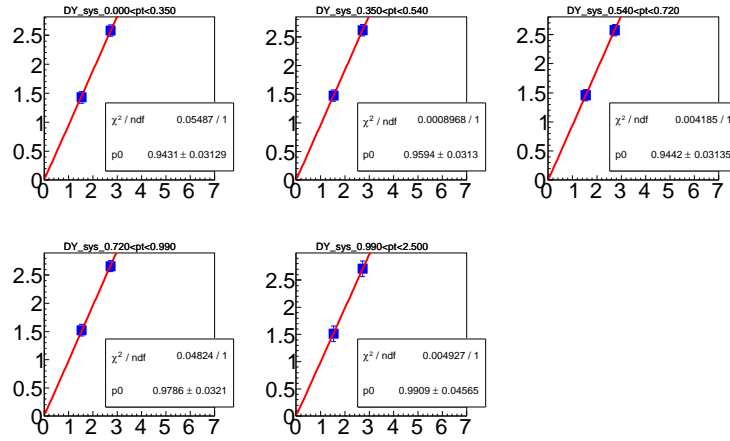
Figure 3.10: The α fitting for each p_T bin for J/Ψ process. The y-axis of figure a is the left part of Eq.3.18 and the x-axis is the right part of Eq. 3.18. This plot shows the fitting without systematic error

Figure 3.11: The α fitting for each p_T bin for J/Ψ process. The y-axis of figure a is the left part of Eq.3.18 and the x-axis is the right part of Eq. 3.18. This plot shows the fitting with systematic error
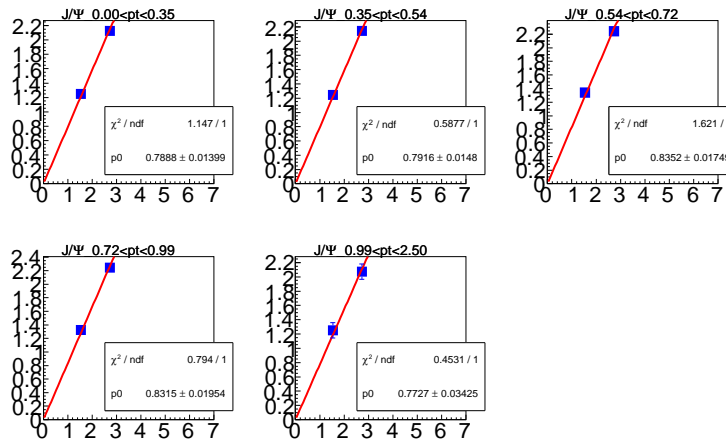
Figure 3.12: The α fitting for each p_T bin for Ψ' process. The y-axis of figure a is the left part of Eq.3.18 and the x-axis is the right part of Eq. 3.18. This plot shows the fitting without systematic error
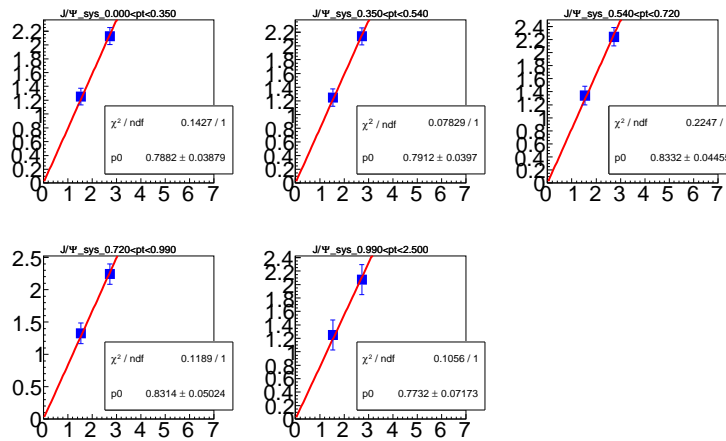

Figure 3.13: The α fitting for each p_T bin for Ψ' process. The y-axis of figure a is the left part of Eq.3.18 and the x-axis is the right part of Eq. 3.18. This plot shows the fitting with systematic error
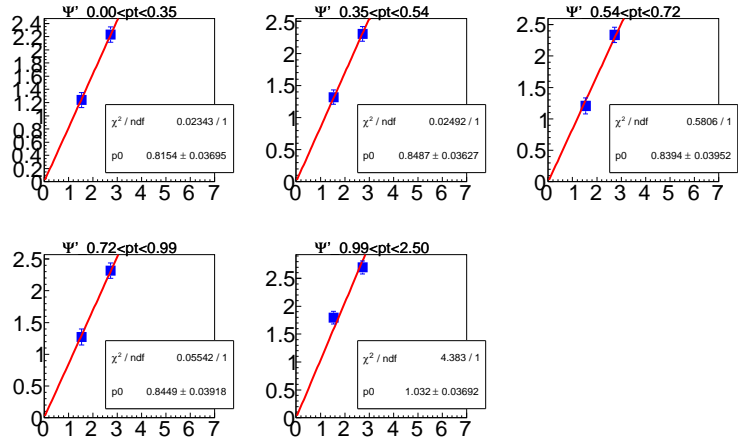
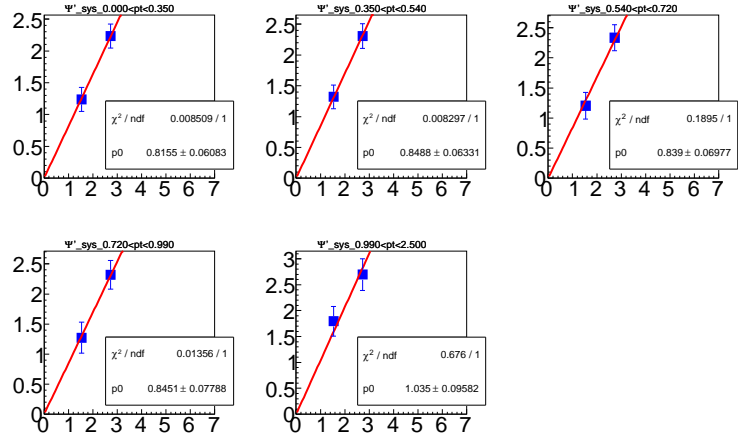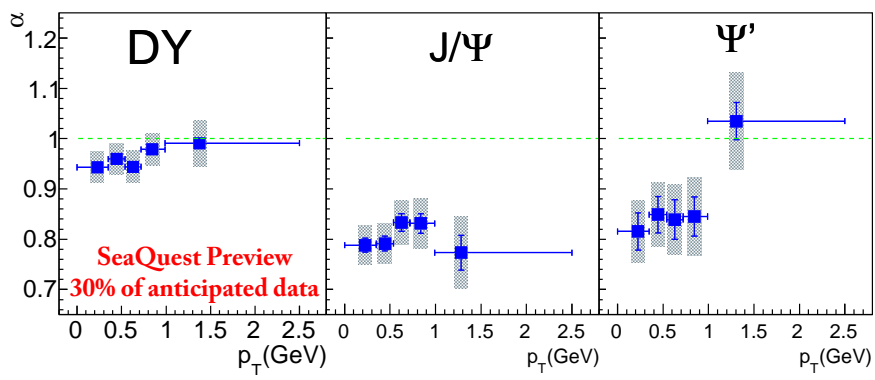Figure 3.14: α result

Chapter 4

Result and Summary

After we got the Ratio and α from the analysis, it is time to compare the E906 result at beam energy at 120 GeV with E772 and E866 at beam energy at 800 GeV. Then we will discuss the difference at the last section.

4.1   Ratio

The ratio of each process is shown in Fig. 4.1. For the DY process, the hallow points are the E772 data[25, 28, 30]. For the J/Ψ and Ψ' the hallow points are the E866 data[26]. The blue points are the E906 data with statistic error. The grey bar is the statistic

error+systematic error. The E906 experiment is using carbon as the reference target; the E772 expriment was using LD2 as the reference target, but the E866 is using Beryllium as the reference target.

Figure 4.1: The Ratio for each process. For the DY process, the hallow points are the E772 data[25, 28, 30]. For the J/Ψ and Ψ' the hallow points are the E866 data[26]. The blue points are the E906 data with statistic error. The grey bar is the statistic error and systematic error. The E906 experiment is using carbon as the reference target; the E772 expriment was using LD2 as the reference target, but the E866 is using Beryllium as the reference target.

4.2 α

The α of each process is shown in Fig 4.2. For the DY process, the hallow points are the E772 data[25, 28, 30]. For the J/Ψ and Ψ' the hallow points are the E866 data[26]. The blue points are the E906 data with statistic error. The grey bar is the statistic error and systematic error. Note. The E906 experiment is using carbon as the reference target; the E772 expriment was using LD2 as the reference target, but the E866 is using beryllium as the reference target.
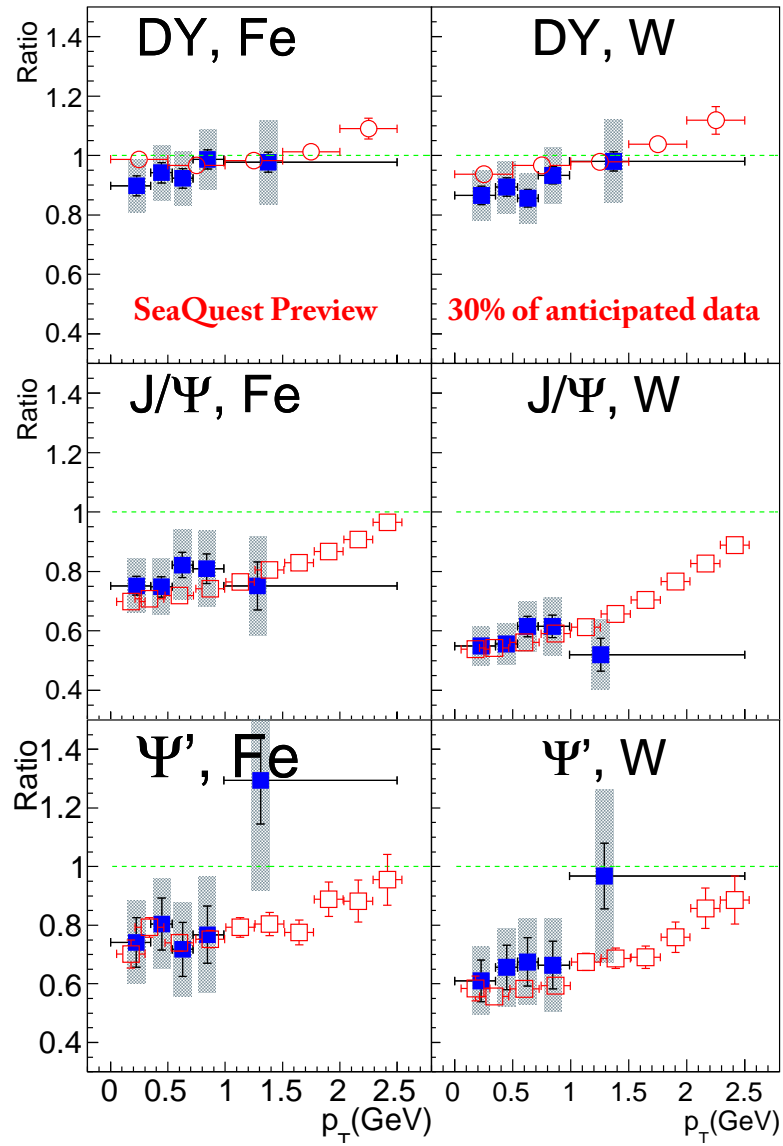

Figure 4.2: The α for each process. For the DY process, the hallow points are the E772 data[25, 28, 30]. For the J/Ψ and Psip the hallow points are the E866 data[26]. The blue points are the E906 data with statistic error. The grey bar is the statistic error + systematic error. Note. The E906 experiment is using carbon as the reference target; the E772 expriment was using LD2 as the reference target, but the E866 is using beryllium as the reference target.
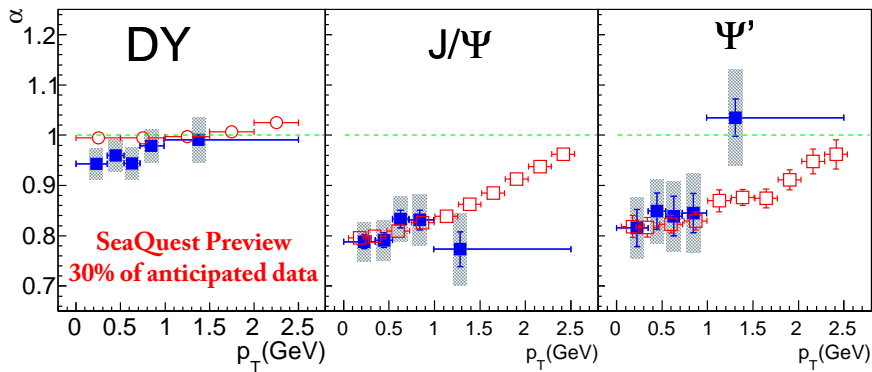
4.3 Conclusion

4.3.1 Drell-Yan process

Compared to J/Ψ and Ψ' there is no strong suppression in DY process. This is expected and also can be used as a controlled check since there is no final-state interaction and only one common production mechanism for DY. The level of p_T suppression of DY is similar in E906 and E866 as expected. However, a slightly suppression at low-p_T regions has been observed. This is consistent with the expectation that lower beam energies will lead to longer interaction time and thus stronger interaction.

4.3.2 J/Ψ and Ψ'

There are no significant differences in the observed strong suppression of J/Ψ and Ψ' with beam energy 800 GeV (E772 and E866) and 120 GeV (E906). Within errors, the nuclear suppression is the same for J/Ψ and Ψ'. This contradicts the assumption while as the radii of J/Ψ and Ψ' differ by almost a factor of 2 in potential models. Production mechanism of J/Ψ and Ψ' remains to be gluon-

gluon interaction because basically the same nuclear-dependence of transverse momentum spectrum is observed.

4.3.3 Baseline for QGP screening

J/Ψ suppression have been observed in the J/Ψ production screening as it is in QGP. However, without the removal of the effects of initial state and final state, it is difficult to justify the effect came from the QGP. As our result is not in the same energy region with QGP, we cannot combine our result with theirs immediately. However, the SeaQuest result does provide the theorists clues of production mechanism, which might help them to develop the theory in the future.

4.3.4 Future improvement

We are working on minimizing systematic uncertainty by finding a better solution of rate dependence. On the statistic side, we will have three times more data from next run. It is also possible to increase J/Ψ and Ψ' events by changing trigger to focus on taking J/Ψ and Ψ' data, which will also reduce huge amounts of background.

Bibliography

[1] E906_Drell-Yan_PAC_2006

[2] http://www.hep.yorku.ca/menary/oldhep/

[3]] J. Pumplin et al., JHEP 07, 012 (2002), hep-ph/0201195.

[4] A. D. Martin, R. G. Roberts, W. J. Stirling, and R. S. Thorne, Eur. Phys. J. C28, 455 (2003), hepph/0211080.

[5] A. D. Martin, R. G. Roberts, W. J. Stirling, and R. S. Thorne, Eur. Phys. J. C35, 325 (2004), hepph/0308087.

[6] M. Gluck, E. Reya, and A. Vogt, Eur. Phys. J. C5, 461 (1998), hep-ph/9806404.

[7] http://hep.pa.msu.edu/cteq/public/ct10.html

[8] http://www.scholarpedia.org/article/   Introduction_to_Parton_Distribution_Functions

[9] http://hep.pa.msu.edu/cteq/public/ct10_2010/figs/

[10] Drell, S.D.; Yan, T.-M. Physical Review Letters 25 (5), (1970),p316–320.

[11] J.W. Qiu, J. P. Vary, and X. f. Zhang, Phys. Rev. Lett. 88, 232301 (2002); Nucl. Phys. A698, 571 (2002).

[12] G. C. Nayak, J.W. Qiu, and G. Sterman, Phys. Rev. Lett. 99, 212001 (2007); Phys. Rev. D 77, 034022 (2008).

[13] Phys. Rev. D 77, 114027 (2008)

[14] T.Matsui. Z. Phys. C - Particles and Fields 38, 245-249 (1988)

[15] T.Matsui,H.Satz,Phys.Lett.B178(1986)416.

[16] C.Baglin,etal.,NA38Collaboration,Phys.Lett.B220(1989)471.

[17] F.Karsch,R.Petronzio,Phys.Lett.B193(1987)105.

[18] J.P.Blaizot,J.-Y.Ollitrault,Phys.Lett.B199(1987)499.

[19] M.C.Chu,T.Matsui,Phys.Rev.D37(1988)1851.

[20] Dmitri Kharzeev, Yuri V. Kovchegov, Kirill Tuchin. Physics
     Letters B 599 (2004) 23–31

[21] B. Abelev et al. (ALICE Collaboration) PRL 110, 082302
     (2013)

[22] PHENIX Collaboration, PRL 111, 202301 (2013)

[23] V. Barger, W.Y. Keung, R.N. Phillips Phys. Lett. B, 91 (1980),
     p. 253

[24] W. Kwong, J. L. Rosner, and C. Quigg, Annu. Rev. Nucl. Part.
     Sci. 37, 325 (1987).

[25] D. M. Alde , Phys. Rev. Lett. 66, 133 (1991); 66, 2285 (1991).

[26] M. J. Leitch et al. (FNAL E866/NuSea Collaboration) Phys.
     Rev. Lett. 84, 3256 – Published 10 April 2000

[27] EMC, J. Ashman et al., Z.Phys. C57 (1993) 211.

[28] D.M. Alde et al., Nuclear Dependence of Dimuon Production
     at 800 GeV, Phys. Rev. Lett. 64, 2479 (1990)

[29] G.T. Garvey and J. C. Peng. Phys. Rev. Lett. 90,9 (2003)

[30] E772 unpublished data, http://p25ext.lanl.gov/e866/papers/e772dy2.html

[31] William M. Lee, A measurement of the Nuclear Dependence of J/ψ and ψ' Production, Georgia State University, 1999 (ps, Fermilab Library)

[32] E906/SeaQuest Spectrometer NIM paper (will be submited at 2016).

[33] T. Zimmerman and J. Hoff. IEEE J. Solid State Circuits. 29, 895-905 (2004)

[34] Moreno, G. et al. Phys. Rev. D, American Physical Society, 1991, 43, 2815-2835

[35] Alde, D. M. et al. Phys. Rev. Lett., American Physical Society, 1990, 64, 2479-2482

[36] Hawker, E. A. & others. Phys. Rev. Lett., American Physical Society, 1998, 80, 3715-3718

[37] Towell, R. S. & others. Phys. Rev., 2001, D64, 052002

[38] Shiuan-Hal Shiu et al (2015). FPGA-based trigger system for the Fermilab SeaQuest experiment. Nucl.Instrum.Meth. A 802, 82.

[39] W.M. Bokhari J.G. Heinrich, N. L. & Newcomer, F. Nuclear Science Symposium, 1998 Conference Record, 1998, 1, 445-446

[40] Jastrzembski, E. VME Trigger Interface. https://userweb.jlab.org/˜moffit/meetings/docs/VmeTIRManual.pdf

[41] Trigger Supervisor v2 (TS) - CODA - Jefferson Lab. https://coda.jlab.org/drupal/system/files/pdfs/HardwareManual/misc/Trigger\%20Supervisor\%20V2.pdf

[42] SIS3610 16 In/16 Output Register. http://www.struck.de/sis3610.htm

[43] 370 Strobed Coincidence. http://www-css.fnal.gov/els/prep/catalog/hardware_info/lecroy/nim/370.html

[44] J. Bouvier, R. Foglio, E. Munoz, O. Rossetto. Internal report to G0-99-017, LPSC 99-10.

[45] Su-Yin Wang, Jinyuan Wu,Shi-Hong Yao,Wen-Chen Chang, Nuclear Science, IEEE Transactions on (Volume:61 , Issue: 6)

[46] ProASIC3 Flash Family FPGAs with Optional Soft ARM Support. [Online]. Available: http://www.actel.com/documents/PA3_DS.pdf

[47] Radiation-Tolerant ProASIC3 FPGAs Radiation Effects. [Online]. Available: http://www.microsemi.com/document-portal/doc_download /131374-radiation-tolerant-proasic3-fpgas-radiation-effects-report

[48] J. Kissel, K. Altwegg, B. C. Clark, "COSIMA – High Resulution Time-Of-Fight Secondary Ion Mass Spectrometer For The Analysis of Cometary Dust Partivles Onboard ROSETTA" Space Science Reviews (2006).

[49] X. Qin, C. Feng, L. Zhao, D. Zhang, S. Liu, X. Hao, Q. An, "Development of High Resolution TDC Implemented in Radiation Tolerant FPGAs for Aerospace Application", IEEE-NPSS Conf. Rec. 2012

[50] Xi Qin, Changqing Feng, Deliang Zhang, Lei Zhao, Shubin Liu, Qi An. "A low dead time vernier delay line TDC implemented in an actel flash-based FPGA", Nucl Sci Tech, vol 24, 040403,2014.

[51] J. Wu "Several key issues on implementing delay line based TDCs using FPGAS", IEEE Trans. Nucl. Sci., vol. 57, no. 3, pp.1543 -1548 2010.

[52] Jian Song, Qi An and Shubin Liu "A high-resolution time-to-digital converter implemented in field-programmable-gate array", IEEE Trans. Nucl. Sci., vol 53, pp 236-241, 2005.

[53] T. Rahkonen and J. Kostamovaara "The use of stabilized CMOS delay lines for the digitization of short time intervals", IEEE J. Solid-State Circuits, vol. 28, no. 8, pp.887 -894 1993.

[54] https://coda.jlab.org/drupal/content/introduction

[55] Kun Liu, DocDB-1283 v1

[56] CBM-SOFT-note-2006-001, by S Gorbunov and I.Kisel

[57] Kun Liu, DocDB-1489 v3

[58] Kun Liu, DocDB-1476 v2

[59] Kenichi's DocDB entry (DocDB-1307), or simply require Spill.dataQuality = 0.

[60] Kun Liu, DocDB-1352-v3

[61] Cranmer KS, Kernel Estimation in High-Energy Physics. 52 // Computer Physics Communications 136:198-207,2001 - e-Print Archive: hep ex/0011057

[62] http://www-bd.fnal.gov/doereview02/RunII_handbook.pdf

[63] SEAQUEST Document 1460-v4

[64] SEAQUEST Document 1493-v11

[65] SEAQUEST Document 1554-v1

[66] SEAQUEST Document 1534-v1